Available online at www.sciencedirect.com
SCIENCE DIRECT®
Journal of Computational Physics 210 (2005) 109–132
JOURNAL OF COMPUTATIONAL PHYSICS
www.elsevier.com/locate/jcp

Fluorescence photon migration by the boundary element method

Francesco Fedele [a], Margaret J. Eppstein [b,*], Jeffrey P. Laible [a], Anuradha Godavarty [c,1], Eva M. Sevick-Muraca [c]

[a] Department of Civil and Environmental Engineering, University of Vermont, Burlington, VT 05405, United States
[b] Department of Computer Science, University of Vermont, Burlington, VT 05405, United States
[c] Photon Migration Laboratories, Department of Chemistry, Texas A&M University, College Station, TX 77842-3012, United States

Received 1 July 2004; received in revised form 5 April 2005; accepted 6 April 2005
Available online 1 June 2005

Abstract

The use of the boundary element method (BEM) is explored as an alternative to the finite element method (FEM) solution methodology for the elliptic equations used to model the generation and transport of fluorescent light in highly scattering media, without the need for an internal volume mesh. The method is appropriate for domains where it is reasonable to assume the fluorescent properties are regionally homogeneous, such as when using highly specific molecularly targeted fluorescent contrast agents in biological tissues. In comparison to analytical results on a homogeneous sphere, BEM predictions of complex emission fluence are shown to be more accurate and stable than those of the FEM. Emission fluence predictions made with the BEM using a 708-node mesh, with roughly double the inter-node spacing of boundary nodes as in a 6956-node FEM mesh, match experimental frequency-domain fluorescence emission measurements acquired on a 1087 cm^3 breast-mimicking phantom at least as well as those of the FEM, but require only 1/8 to 1/2 the computation time.

Keywords: Boundary element method; Frequency domain photon migration; Flourescence tomography; Coupled elliptic equations

* Corresponding author. Tel.: +1 802 656 1918; fax: +1 802 656 0696.
E-mail address: maggie.eppstein@uvm.edu (M.J. Eppstein).
[1] Present address: Department of Biomedical Engineering, Florida International University, Miami, FL 33174, United States.

0021-9991/$ - see front matter © 2005 Elsevier Inc. All rights reserved.
doi:10.1016/j.jcp.2005.04.003

1. Introduction

Imaging plays a central part of cancer diagnosis, therapy, and prognosis primarily through the detection of anatomically defined abnormalities. With the wealth of information provided by the now maturing areas of genomics and proteomics, the identification of molecular markers and targets now promises contrast-enhanced, diagnostic imaging with specificity and sensitivity that is not otherwise possible with conventional, anatomical imaging. Molecular imaging promises to improve diagnostic imaging and to impact the quality of cancer patient care.

Near-infrared (NIR) light between the wavelengths of 700 and 900 nm propagates deeply through tissues and provides a unique approach for molecularly based diagnostic imaging. In the past decade, significant progress has been made in developing molecularly targeted fluorescent dyes for molecular imaging [1–7]. With near-infrared excitable fluorescent contrast agents that can be conveniently conjugated with a targeting or reporting moiety, there is potential clinical opportunity for using non-ionizing radiation with these non-radioactive contrast agents for "homing in" on early metastatic lesions, performing sentinel lymph node mapping, and following the progress of therapy.

Direct imaging of fluorescence is possible in small animal and near-surface applications. However, in order to quantify fluorochrome concentrations and/or to image fluorescent targets deeper into tissues, where the rapid decay of light renders the diffuse signal weak and noisy, tomographic reconstruction is necessary. Three-dimensional fluorescence tomography has recently been demonstrated in both for near-surface targets [8–10] and deeper targets [11–16], from experimentally acquired measurements. However, especially in large volumes, there remain a number of challenges for obtaining reliably quantitative and highly resolved image reconstructions, as outlined below.

In NIR fluorescence-enhanced tomography [17], the tissue surface is illuminated with excitation light and measurements of fluorescent light emission are collected at the tissue surface. A forward model of fluorescent light generation and transport through tissue is used to predict the observable states (e.g., emission fluence) at the measurement locations, based on the known excitation light source and an estimate of spatially distributed optical properties of the tissue volume. A computational implementation of the forward model is typically used repeatedly within an inverse (tomography) method, wherein estimates of spatially distributed optical properties of the tissue are iteratively updated until the predictions match the observations sufficiently well, or some other convergence criteria is achieved. Consequently, a rapid and accurate implementation of the forward model is critical for a rapid and accurate tomography code.

In clinically relevant volumes of highly scattering media, the forward problem of fluorescent light generation and transport can be effectively approximated as a diffusive process. The generation and propagation of fluorescent light through highly scattering media (such as biological tissues) is often modeled by a pair of second order, elliptic, partial differential equations [18–20]. The first equation represents propagation of excitation light (subscript x) and the second models the generation and propagation of fluorescently emitted light (subscript m). Herein, we focus on frequency domain measurements using intensity modulated illumination, because (a) these time-dependent measurements permit the implementation of fluorescence lifetime tomography [16], and (b) frequency domain measurements have some advantages over time domain measurements approaches, including that ambient light rejection is automatic and does not require background subtraction. In the frequency domain, the diffusion approximations to the radiative transport equation over a three-dimensional (3D) bounded domain Ω are

$$-\nabla\cdot(D_x\nabla\Phi_x)+k_x\Phi_x=S_x, \tag{1}$$

$$-\nabla\cdot(D_m\nabla\Phi_m)+k_m\Phi_m=\beta\Phi_x \tag{2}$$

subject to the Robin boundary conditions on the domain boundary $\partial\Omega$ of

$$\vec{n}\cdot(D_x\nabla\Phi_x)+b_x\Phi_x=p_x, \tag{3}$$

$$\vec{n}\cdot(D_m\nabla\Phi_m)+b_m\Phi_m=0, \tag{4}$$

where ∇ is the 3D (3×1) grad operator and $\vec{n}$ is the 3D (3×1) vector normal to the boundary. In fluorescence tomography the light source is localized on the surface and thus it can be modeled either by an appropriate definition of excitation light source S_x (W/cm^3) or as a source flux p_x (W/cm^2) on the surface boundary. Sources are intensity modulated with sinusoidal frequency ω (rad/s), and propagate through the media resulting in the AC component of complex photon fluence at the excitation wavelength of Φ_x (W/cm^2). The diffusion ($D_{x,m}$), decay ($k_{x,m}$), and emission source (β) coefficients, as shown below,

$$\begin{cases} D_x=\frac{1}{3(\mu_{\mathrm{a}xi}+\mu_{\mathrm{a}xf}+\mu'_{\mathrm{s}x})}, \\ D_m=\frac{1}{3(\mu_{\mathrm{a}mi}+\mu_{\mathrm{a}mf}+\mu'_{\mathrm{s}m})}, \end{cases} \quad \begin{cases} k_x=\frac{\mathrm{i}\omega}{c}+\mu_{\mathrm{a}xi}+\mu_{\mathrm{a}xf}, \\ k_m=\frac{\mathrm{i}\omega}{c}+\mu_{\mathrm{a}mi}+\mu_{\mathrm{a}mf}, \end{cases} \quad \beta=\frac{\phi\mu_{\mathrm{a}xf}}{1-\mathrm{i}\omega\tau} \tag{5}$$

are functions of absorption coefficients due to non-fluorescing chromophore ($\mu_{\mathrm{a}xi},\mu_{\mathrm{a}mi}$), absorption coefficients due to fluorophore ($\mu_{\mathrm{a}xf},\mu_{\mathrm{a}mf}$), and isotropic (reduced) scattering coefficients ($\mu'_{\mathrm{s}x},\mu'_{\mathrm{s}m}$) at the two wavelengths (all in units of cm^{-1}), fluorescence quantum efficiency (ϕ), and fluorescence lifetime (τ, in s). Here, $\mathrm{i}=\sqrt{-1}$, and c is the speed of light in the media (cm/s). The Robin boundary coefficients (b_x,b_m) are governed by the reflection coefficients (R_x,R_m), which range from 0 (no reflectance) to 1 (total reflectance):

$$b_x=\frac{1-R_x}{2(1+R_x)}, \quad b_m=\frac{1-R_m}{2(1+R_m)}. \tag{6}$$

In diffuse fluorescence tomography, the forward model is commonly computationally implemented using the finite element method (FEM) [13,21,22]. Despite the fact that all excitation sources and detected measurements are restricted to the tissue surface, in the FEM the entire volume must be discretized into nodes and 3D elements. The internal FEM mesh makes it straightforward to implement the internally distributed emission source term ($\beta\Phi_x$). Unfortunately, the internal FEM mesh introduces discretization error that can render the method unstable, unless a fine enough mesh is employed. In biological tissues, the rate of decay (k, dominated by the absorption coefficients μ_{a}) is typically much larger than the rate of diffusion (D, dominated by the inverse of the scattering coefficients μ'_{s}, where $\mu'_{\mathrm{s}}\gg\mu_{\mathrm{a}}$), so fine internal volume meshes are required in order to achieve a smooth and stable result. Furthermore, the spatial resolution of small internal targets is governed by the internal mesh discretization in a FEM model. In a tomography algorithm, where the target locations are unknown in advance, fine target resolution in an FEM-based tomography code will require either a uniformly fine mesh or an adaptive meshing scheme, both of which add to the computational complexity of the model. If the optical parameters to be estimated in a tomographic reconstruction are associated with internal nodes or elements, the inverse problem of FEM-based tomographic reconstruction algorithm will be highly underdetermined, since the number of nodes or elements in an adequately resolved FEM mesh typically far exceeds the number of surface measurements available for inversion [12,14,15]. In fluorescence tomography applications for large volumes this problem is exacerbated because a very fine mesh resolution imposes large computational memory and time requirements that may be impractical, and because the signal-to-noise of fluorescence emission measurements in large volumes is extremely low and highly spatially variant [11,12], thereby rendering the inverse problem even more ill-posed. There have been a variety of weighting and damping approaches proposed for regularization of ill-posed FEM tomography codes [11,23–26], as well as methods that explicitly reduce the dimensionality of the parameter space in various FEM-based tomographic applications, including (i) use of a priori structural information from co-registered magnetic resonance images to reduce the number of uncertain optical parameters [27], (ii) use of clustering algorithms to dynamically merge spatially adjacent uncertain

parameters based on their evolving estimates between iterations (aka data-driven zonation) [11,28,29], and (iii) use of adaptive mesh refinement to enable use of a relatively coarse mesh in the background while increasing spatial resolution inside regions of interest, based on evolving estimates [30]. Although these regularization approaches have made FEM-based fluorescence tomography possible, it must be noted that accuracy of FEM-based tomography is sensitive to the regularization imposed.

These difficulties associated with FEM-based fluorescence tomography motivate us to explore boundary element method (BEM)-based tomography, wherein the BEM [31] is used as an alternative numerical approach for solving the diffusion approximations to excitation and emission radiative transport (1) and (2). In the 3D BEM, the domain is modeled with a finite number of spatially coherent 3D regions, each of which is considered homogeneous. Only the boundaries of these subdomains must be discretized into nodes and two-dimensional (2D) elements. Inside each subdomain analytical solutions are employed, with compatibility and equilibrium constraints enforced on shared boundaries between subdomains [31]. For domains in which it is reasonable to assume that parameters can be modeled with a relatively small number of regionally homogeneous subdomains, the BEM thus requires many fewer nodes and elements than the FEM, and is subject to less discretization error.

A BEM forward model of fluorescent light generation and propagation is expected to provide increases in accuracy over the FEM in circumstances where it is reasonable to assume regional homogeneity of fluorescent properties. We postulate that this will be the case for some biomedical fluorescence tomography applications using highly selective molecularly targeting and reporting dyes. When using receptor-targeted fluorescent markers, fluorescent properties such as absorption and lifetime will tend to be highly localized (e.g., on the surface of a discrete tumor) and may therefore be conducive to BEM modeling. While endogenous optical absorption and scattering will remain much more spatially heterogeneous that the distribution of fluorophore, the change in time-dependent measurements with physiological absorption and scattering contrast is insignificant in comparison to the change owing to the fluorescence decay kinetics. Indeed, signal perturbations due to endogenous levels of scattering and absorption contrast can be within the measurement error of time-dependent measurements. Prior computational studies using synthetic data have confirmed that tomographic inversion of fluorescence emission fluence is relatively insensitive to a wide range of unmodeled variability in background absorption and scattering [29].

In order for BEM-based fluorescence tomography to be successfully applied, it is necessary to have an independent means of initially estimating the approximate number and locations of regions to be estimated, such as with a second imaging modality or reconstruction technique. We outline several possible approaches below. For example, direct fluorescent images of small animals [32], or co-registered PET or MRI images in deeper tissues using multimodal contrast agents [33], could be used to provide a priori estimates of target location and geometry. In these cases, only the quantitative optical properties of the target(s) would need to be estimated, resulting in many fewer unknowns than measurements. In other applications, it may be reasonable to assume a simple target geometry (e.g., a sphere) and simply estimate the optical properties and centroid location of the target (e.g., in sentinel lymph node imaging, where the primary goal is to locate the node [34]). In the more general case, the location, geometry, and optical properties of targets must be estimated. This could be accomplished by estimating the locations of the boundary element nodes on the internal subdomains in addition to the optical parameters inside the various subdomains. This form of BEM-based tomography has already been successfully demonstrated in electrical impedance tomography [35,36]. An approach that has proven successful in BEM-based electrical impedance tomography alternates several generations of a genetic algorithm with several iterations of a gradient-based local optimizer, to dynamically determine the number, locations, and geometries of internal subdomains [36]. Other approaches that may prove effective for providing an initial estimate of target numbers and locations for subsequent refinement with a BEM tomographic reconstruction include (i) extracting approximate parameter structure from the result of a small number of iterations of an FEM-based tomographic reconstruction, (ii) using an artificial neural network (e.g., a radial basis function neural network

[37]) for rapid initial approximation of parameter structure, or (iii) using *a priori* parameter structure estimates from other co-registered imaging modalities, such as PET or MRI. Alternatively, targets could be added in sequentially until an optimal solution is reached. In general, in comparison to FEM-based tomography, BEM-based tomographic reconstructions are likely to have (i) fewer unknowns and be overdetermined rather than underdetermined, (ii) greater flexibility regarding modeling the geometries of discrete internal targets, and (iii) less discretization error internal to homogeneous regions. Hence, for applications in which one can estimate where to locate internal boundaries, BEM-based fluorescence tomography may yield more accurate parameter estimates, that are less sensitive to selection of regularization parameters, and in less computational time, than FEM-based fluorescence tomography.

There are reports in the literature of successful applications of the BEM to the optical excitation equation (1) [38] and to the electrical impedance diffusion equation [35,36]. In these applications, implementation of the BEM is relatively straightforward, since all sources and detectors are located on the surface of the domain, where the BEM must be discretized in any case. However, modeling fluorescently generated light, emitted from an internal target, is not straightforward with the BEM. In this case, the source term for the emission equation (2) is internally distributed; it is non-zero wherever there is non-zero fluorescence absorption coefficient (μ_{axf}, μ_{amf}). Modeling this internal source term without an explicit internal volume mesh makes application of the BEM non-trivial. We have found no prior references to the BEM for the coupled excitation/emission equations (1) and (2). In this contribution, we develop and validate a solution to this problem that does not require any internal volume mesh.

Ultimately, we plan to explore various approaches for a practical BEM implementation for 3D fluorescence tomography, as well as BEM–FEM hybrid approaches. As a first step towards BEM-based fluorescence tomography, we herein report on the derivation, implemention, and validation of a prototype BEM forward model of the generation and propagation of fluorescent light through highly scattering media.

2. BEM formulation for the governing equations

The governing equations (1) and (2) are only coupled in one direction; that is, the solution to Eq. (2) depends on the solution to Eq. (1), but not vice versa. Consequently, it is possible to solve these equations sequentially. To predict fluorescence emission fluence Φ_m at surface detectors (generated in response to an excitation source S_x also at the tissue surface), one first solves the excitation equation (1) with the boundary conditions (3), to predict excitation fluence Φ_x at all the nodes in the domain volume Ω. The predicted excitation fluence is subsequently used in the source term ($\beta\Phi_x$) for solving the emission equation (2), subject to boundary conditions (4), for emission fluence Φ_m. Since an internal discretization of the entire volume Ω is already a requirement of the FEM, the internally distributed source term for Eq. (2) requires no special accommodation. However, if a sequential solution approach were employed in a BEM formulation, this would necessitate the creation of an internal mesh for the BEM in order to represent the internally distributed fluorescent source. This approach would eliminate many of the potential advantages of the BEM over the FEM.

Alternatively, one can entirely preclude the need of an internal volume mesh discretization when using BEM if the governing equations (1) and (2) are solved simultaneously, rather than sequentially. We recast the governing equations into the following matrix form:

$$-\underline{\underline{\nabla}}^{\mathrm{T}}(\underline{\underline{\mathbf{D}}}\underline{\underline{\nabla}}\underline{\mathbf{\Phi}}) + \underline{\mathbf{k}}\underline{\mathbf{\Phi}} = \underline{\mathbf{S}} \quad \text{on } \Omega. \tag{7}$$

Similarly, the boundary conditions (3) and (4) are represented by the matrix equation

$$\underline{\mathbf{n}}^{\mathrm{T}}(\underline{\underline{\mathbf{D}}}\underline{\underline{\nabla}}\underline{\mathbf{\Phi}}) + \underline{\mathbf{r}}\underline{\mathbf{\Phi}} = \underline{\mathbf{p}} \quad \text{on } \partial\Omega. \tag{8}$$

Here, we distinguish vector quantities with a single underbar and matrix quantities with a double underbar and we use the following matrix definitions:

$$\underset{(6\times2)}{\underline{\underline{\nabla}}} = \begin{bmatrix} \nabla & \underline{0} \\ \underline{0} & \nabla \end{bmatrix}, \quad \underset{(6\times2)}{\underline{\underline{\mathbf{n}}}} = \begin{bmatrix} \vec{n} & \underline{0} \\ \underline{0} & \vec{n} \end{bmatrix}, \quad \underset{(6\times6)}{\underline{\underline{\mathbf{D}}}} = \begin{bmatrix} D_x \underset{(3\times3)}{\underline{\underline{\mathbf{I}}}} & \underline{\underline{0}} \\ \underline{\underline{0}} & D_m \underset{(3\times3)}{\underline{\underline{\mathbf{I}}}} \end{bmatrix}, \quad \underset{(2\times2)}{\underline{\underline{\mathbf{k}}}} = \begin{bmatrix} k_x & 0 \\ -\beta & k_m \end{bmatrix},$$
$$\underset{(2\times2)}{\underline{\underline{\mathbf{r}}}} = \begin{bmatrix} b_x & 0 \\ 0 & b_m \end{bmatrix}, \quad \underset{(2\times1)}{\underline{\underline{\mathbf{\Phi}}}} = \begin{bmatrix} \Phi_x \\ \Phi_m \end{bmatrix}, \quad \underset{(2\times1)}{\underline{\underline{\mathbf{S}}}} = \begin{bmatrix} S_x \\ 0 \end{bmatrix}, \quad \underset{(2\times1)}{\underline{\underline{\mathbf{p}}}} = \begin{bmatrix} p_x \\ 0 \end{bmatrix}, \tag{9}$$

where $\underline{\underline{\mathbf{I}}}$ is the identity matrix. The sizes of each matrix are shown for clarity. Note that in the matrix formulation above we have moved the emission source term ($\beta\Phi_x$) to the left-hand side of the emission equation. We first present a BEM solution to system (7) on homogeneous domains, and then extend this to the case of non-homogeneous domains.

2.1. Homogenous domains

By assuming a homogenous domain, where the matrices $\underline{\underline{\mathbf{D}}}$, $\underline{\underline{\mathbf{k}}}$, $\underline{\underline{\mathbf{b}}}$ are spatially constant inside the domain Ω, we can rewrite Eq. (7) as follows:

$$-\nabla^2\underline{\mathbf{\Phi}} + \underline{\underline{\mathbf{K}}}\underline{\mathbf{\Phi}} = \underline{\mathbf{S}} \quad \text{on } \Omega \tag{10}$$

with

$$\underset{(2\times2)}{\underline{\underline{\mathbf{K}}}} = \left[\underline{\underline{\mathbf{D}}}^{-1}\underline{\underline{\mathbf{k}}}\right], \quad \underset{(2\times1)}{\underline{\tilde{\mathbf{S}}}} = \left[\underline{\underline{\mathbf{D}}}^{-1}\underline{\mathbf{S}}\right]. \tag{11}$$

Here, $\underline{\underline{\mathbf{X}}}^{-1}$ indicates the inverse of the matrix $\underline{\underline{\mathbf{X}}}$.

We now define an arbitrary matrix of functions $\underline{\underline{\mathbf{\Psi}}}$

$$\underset{(2\times2)}{\underline{\underline{\mathbf{\Psi}}}} = \begin{bmatrix} \Psi_{xx} & \Psi_{xm} \\ \Psi_{mx} & \Psi_{mm} \end{bmatrix}. \tag{12}$$

Multiplying Eq. (10) by the transpose of $\underline{\underline{\mathbf{\Psi}}}$ and integrating over the entire domain Ω yields

$$\int_\Omega \underline{\underline{\mathbf{\Psi}}}^{\mathrm{T}}(-\nabla^2\underline{\mathbf{\Phi}} + \underline{\underline{\mathbf{K}}}\underline{\mathbf{\Phi}})\,\mathrm{d}\underline{\mathbf{x}} = \int_\Omega \underline{\underline{\mathbf{\Psi}}}^{\mathrm{T}}\underline{\tilde{\mathbf{S}}}\,\mathrm{d}\underline{\mathbf{x}}, \tag{13}$$

where superscript T indicates the transpose operator. Integrating by parts twice and incorporating the boundary conditions (8) gives

$$\int_\Omega (-\nabla^2\underline{\underline{\mathbf{\Psi}}} + \underline{\underline{\mathbf{K}}}^{\mathrm{T}}\underline{\underline{\mathbf{\Psi}}})^{\mathrm{T}}\mathbf{\Phi}\,\mathrm{d}\underline{\mathbf{x}} + \int_{\partial\Omega}\left(-\underline{\underline{\mathbf{\Psi}}}^{\mathrm{T}}\frac{\partial\underline{\mathbf{\Phi}}}{\partial n} + \frac{\partial\underline{\underline{\mathbf{\Psi}}}^{\mathrm{T}}}{\partial n}\underline{\mathbf{\Phi}}\right)\mathrm{d}\underline{\mathbf{x}} = \int_\Omega \underline{\underline{\mathbf{\Psi}}}^{\mathrm{T}}\underline{\tilde{\mathbf{S}}}\,\mathrm{d}\underline{\mathbf{x}}. \tag{14}$$

We now define the matrix $\underline{\underline{\mathbf{\Psi}}}$ such that the following adjoint equation is satisfied, that is

$$-\nabla^2\underline{\underline{\mathbf{\Psi}}} + \underline{\underline{\mathbf{K}}}^{\mathrm{T}}\underline{\underline{\mathbf{\Psi}}} = \underline{\underline{\Delta}}_j. \tag{15}$$

We define $\rho = |\underline{\mathbf{x}} - \underline{\mathbf{x}}_j|$ to be the distance from any arbitrary point $\underline{\mathbf{x}}$ in the domain to the jth node, $\underline{\mathbf{x}}_j$. Then, $\underline{\underline{\Delta}}_j$ is a 2×2 diagonal matrix of Dirac delta functions centered at node j,

$$\underset{(2\times2)}{\underline{\underline{\Delta}}_j} = \begin{bmatrix} \delta(\rho) & 0 \\ 0 & \delta(\rho) \end{bmatrix}. \tag{16}$$

Hereafter $\underline{\underline{\Psi}}$ is called the Green matrix of the 3D diffusion equations (7) in an infinite domain (equivalent to the Green's function for the scalar case).

Eq. (14) then simplifies as follows:

$$\underline{\Phi}(\underline{x}_d) + \int_{\partial\Omega} \left(-\underline{\underline{\Psi}}^{\mathrm{T}} \frac{\partial \underline{\Phi}}{\partial n} + \frac{\partial \underline{\underline{\Psi}}^{\mathrm{T}}}{\partial n} \underline{\Phi} \right) \mathrm{d}\underline{x} = \int_{\Omega} \underline{\underline{\Psi}}^{\mathrm{T}} \underline{\tilde{S}} \, \mathrm{d}\underline{x}. \tag{17}$$

A modal decomposition procedure is applied to solve the system (15) (see Appendix A for details) which yields, for the case of fluorescence photon migration, the following analytical expression for $\underline{\underline{\Psi}}$

$$\underline{\underline{\Psi}} = \begin{bmatrix} G\left(\sqrt{-\frac{k_x}{D_x}}\rho\right) & \frac{G\left(\sqrt{-\frac{k_x}{D_x}}\rho\right) - G\left(\sqrt{-\frac{k_m}{D_m}}\rho\right)}{\frac{D_m}{\beta}\left(\frac{k_x}{D_x} - \frac{k_m}{D_m}\right)} \\ 0 & G\left(\sqrt{-\frac{k_m}{D_m}}\rho\right) \end{bmatrix}. \tag{18}$$

Note that, for the fluorescence photon migration case, the component Ψ_{mx} of the matrix $\underline{\underline{\Psi}}$ is zero, reflecting the asymmetry in the governing equations (1) and (2); that is, Φ_x influences Φ_m, but not vice versa. In Eq. (18), $G(\sqrt{-\lambda}\rho)$ is the scalar Green's function satisfying the Helmholtz equation

$$\nabla^2 G - \lambda G + \delta(\rho) = 0, \quad \lambda = \frac{k_x}{D_x}, \frac{k_m}{D_m}. \tag{19}$$

For 3D domains, the function G is defined as:

$$G(\sqrt{-\lambda}\rho) = \frac{1}{4\pi\rho} \exp(\mathrm{i}\sqrt{-\lambda}\rho). \tag{20}$$

(See Appendix A for the 2D case.) The integral equation (17) can be solved by BEM discretization as follows. We first consider a triangular mesh discretization Υ_h of the boundary $\partial\Omega$. Without loss of generality, we illustrate with linear elements. Over the boundary $\partial\Omega$, we define the real finite functional space

$$V_h = \{u|_K \in C^0(\partial\Omega)\}, \tag{21}$$

where $u|_K$ is a linear polynomial, $K \in \Upsilon_h$ is the generic surface triangular element, and $h = \max_{K \epsilon \Upsilon_h} \mathrm{diam}(K)$ is the maximal dimension of the element. We define the global bases for $V_h(\partial\Omega)$ as $\{N_1, N_2, \ldots, N_n\}$, where n is the number of nodes. The generic basis elements are defined such that $N_i(\underline{x}_j) = \delta_{ij}$ with δ_{ij} the Kronecker symbol. By means of these bases, the fluence $\underline{\Phi}$, its normal derivative $\underline{q} = \frac{\partial \underline{\Phi}}{\partial n}$, and the boundary flux $\underline{p}$ can be approximated as

$$\underline{\Phi}(\underline{x}) = \sum_{k=1}^{n} N_k(\underline{x}) \underline{\Phi}_k, \quad \underline{q}(\underline{x}) = \sum_{k=1}^{n} N_k(\underline{x}) \underline{q}_k, \quad \underline{p}(\underline{x}) = \sum_{k=1}^{n} N_k(\underline{x}) \underline{p}_k, \tag{22}$$

where $\underline{\Phi}_k$, $\underline{q}_k$ and $\underline{p}_k$ indicate values relative to the node k. Using these approximations and choosing $\underline{x}_j$ to span all the nodes of the surface Υ_h, i.e., $\underline{x}_j = \underline{x}_i \; \forall i = 1, \ldots, n$, Eqs. (17) and (8) give, respectively, the following set of algebraic equations:

$$\underline{\underline{\mathbf{H}}}\,\underline{\mathscr{U}} + \underline{\underline{\mathbf{G}}}\,\underline{\mathscr{V}} = \underline{\mathscr{S}}, \tag{23}$$

$$\underline{\mathscr{V}} = -\underline{\underline{\mathbf{R}}}\,\underline{\mathscr{U}} + \underline{\mathbf{P}}. \tag{24}$$

The matrix $\underline{\underline{\mathbf{R}}}$ is block-diagonal of dimension $(2n \times 2n)$, with n the number of nodes, as follows:

$$\underset{(2n\times 2n)}{\underline{\underline{\mathbf{R}}}} = \begin{bmatrix} \underline{\underline{\mathbf{r}}} & & \\ & \underline{\underline{\mathbf{r}}} & \cdots \\ & \cdots & \\ & & \underline{\underline{\mathbf{r}}} \end{bmatrix}. \tag{25}$$

We define $\underset{(2n\times 1)}{\underline{\mathscr{U}}}$, $\underset{(2n\times 1)}{\underline{\mathscr{V}}}$, $\underset{(2n\times 1)}{\underline{\mathbf{P}}}$ and $\underset{(2n\times 1)}{\underline{\mathscr{S}}}$ as the column vectors of the nodal values of the fluence $\underline{\mathbf{\Phi}}$, its normal derivative $\underline{\mathbf{q}}$, the prescribed boundary flux $\underline{\mathbf{p}}$ and the volume source $\underline{\mathbf{S}}$, respectively. These are vectors of dimension $(2n\times 1)$, i.e.,

$$\underset{(2n\times 1)}{\underline{\mathscr{U}}} = \begin{bmatrix} \underline{\mathbf{\Phi}}_1 \\ \cdots \\ \cdots \\ \underline{\mathbf{\Phi}}_n \end{bmatrix}, \quad \underset{(2n\times 1)}{\underline{\mathscr{V}}} = \begin{bmatrix} \underline{\mathbf{q}}_1 \\ \cdots \\ \cdots \\ \underline{\mathbf{q}}_n \end{bmatrix}, \quad \underset{(2n\times 1)}{\underline{\mathbf{P}}} = \begin{bmatrix} \underline{\mathbf{p}}_1 \\ \cdots \\ \cdots \\ \underline{\mathbf{p}}_n \end{bmatrix}, \quad \underset{(2n\times 1)}{\underline{\mathscr{S}}} = \begin{bmatrix} \underline{\mathbf{s}}_1 \\ \cdots \\ \cdots \\ \underline{\mathbf{s}}_n \end{bmatrix}, \tag{26}$$

where the (2×1) vector component $\underline{\mathbf{s}}_j$ at each node j is given by

$$\underset{(2\times 1)}{\underline{\mathbf{s}}_j} = -\int_{\Omega} \underline{\underline{\mathbf{\Psi}}}^{\mathrm{T}}(\rho)\underline{\mathbf{S}}(\underline{\mathbf{x}})\,\mathrm{d}\Omega. \tag{27}$$

In the case of a point source located on the surface of a 3D domain, we effectively use a lumped mass matrix to concentrate the source at a specific point $\underline{\mathbf{x}}_s$ located one scattering length inside and normal to the surface beneath the point source, so the integral in Eq. (27) disappears as follows:

$$\underset{(2\times 1)}{\underline{\mathbf{s}}_j} = -\underline{\underline{\mathbf{\Psi}}}^{\mathrm{T}}(|\underline{\mathbf{x}}_j - \underline{\mathbf{x}}_s|)\underline{\mathbf{S}}(\underline{\mathbf{x}}_s). \tag{28}$$

By relocating the point source just inside the domain (so $\underline{\mathbf{x}}_j \neq \underline{\mathbf{x}}_s\ \forall j,s$) we avoid singularities arising from source locations that coincide with a boundary node. The BEM matrices $\underline{\underline{\mathbf{H}}}$, $\underline{\underline{\mathbf{G}}}$ are partitioned as

$$\underset{(2n\times 2n)}{\underline{\underline{\mathbf{H}}}} = \begin{bmatrix} \underline{\underline{\mathbf{h}}}_{11} & \underline{\underline{\mathbf{h}}}_{12} & \cdots & \underline{\underline{\mathbf{h}}}_{1n} \\ & \cdots & \cdots & \\ & \cdots & \underline{\underline{\mathbf{h}}}_{jk} & \cdots \\ & & \cdots & \underline{\underline{\mathbf{h}}}_{nn} \end{bmatrix}, \quad \underset{(2n\times 2n)}{\underline{\underline{\mathbf{G}}}} = \begin{bmatrix} \underline{\underline{\mathbf{g}}}_{11} & \underline{\underline{\mathbf{g}}}_{12} & \cdots & \underline{\underline{\mathbf{g}}}_{1n} \\ & \cdots & \cdots & \\ & \cdots & \underline{\underline{\mathbf{g}}}_{jk} & \cdots \\ & & \cdots & \underline{\underline{\mathbf{g}}}_{nn} \end{bmatrix}, \tag{29}$$

where the block elements are computed as follows:

$$\underset{(2\times 2)}{\underline{\underline{\mathbf{h}}}_{jk}} = \delta_{jk}\underset{(2\times 2)}{\underline{\underline{\mathbf{I}}}} + \int_{\partial\Omega} \frac{\partial \underline{\underline{\mathbf{\Psi}}}^{\mathrm{T}}(\rho)}{\partial n} N_k(\underline{\mathbf{x}})\,\mathrm{d}\underline{\mathbf{x}}, \tag{30}$$

$$\underset{(2\times 2)}{\underline{\underline{\mathbf{g}}}_{jk}} = -\int_{\partial\Omega} \underline{\underline{\mathbf{\Psi}}}^{\mathrm{T}}(\rho)N_k(\underline{\mathbf{x}})\,\mathrm{d}\underline{\mathbf{x}}. \tag{31}$$

Remark 1. Note that, since the component Ψ_{mx} of the Green matrix $\underline{\underline{\mathbf{\Psi}}}$ is zero [see Eq. (18)], the resulting matrices $\underline{\underline{\mathbf{H}}}$ and $\underline{\underline{\mathbf{G}}}$ are 3/4 populated $2n\times 2n$ matrices, where n is the number of nodes in the BEM mesh. By defining $\underline{\mathbf{\Phi}}_x$ and $\underline{\mathbf{\Phi}}_m$ as column vectors of the nodal values of the fluences Φ_x and Φ_m, the vectors $\underline{\mathscr{U}}$ and $\underline{\mathscr{V}}$ can be rearranged as follows:

$$\underset{(2n\times 1)}{\underline{\mathscr{U}}} = \begin{bmatrix} \underline{\mathbf{\Phi}}_x \\ \underline{\mathbf{\Phi}}_m \end{bmatrix}, \quad \underset{(2n\times 1)}{\underline{\mathscr{V}}} = \begin{bmatrix} \underline{\mathbf{q}}_x \\ \underline{\mathbf{q}}_m \end{bmatrix} \tag{32}$$

and one finds that the matrices $\underline{\underline{\mathbf{H}}}$ and $\underline{\underline{\mathbf{G}}}$ in Eq. (23) have the following structure:

$$\underline{\underline{\mathbf{H}}} = \begin{bmatrix} \underline{\underline{\mathbf{H}}}_{xx} & \underline{\underline{\mathbf{0}}} \\ \underline{\underline{\mathbf{H}}}_{xm} & \underline{\underline{\mathbf{H}}}_{mm} \end{bmatrix}, \quad \underline{\underline{\mathbf{G}}} = \begin{bmatrix} \underline{\underline{\mathbf{G}}}_{xx} & \underline{\underline{\mathbf{0}}} \\ \underline{\underline{\mathbf{G}}}_{xm} & \underline{\underline{\mathbf{G}}}_{mm} \end{bmatrix}. \tag{33}$$

For a given surface mesh, the size of the BEM matrices is smaller (dimensioned by number of boundary nodes times 2) than the size of the FEM matrices for the excitation and emission equations (dimensioned by number of nodes in the FEM volume mesh). The computation of the matrix block element entries (Eqs. (30) and (31)) can be done using Gauss integration (we used seven collocation points inside each triangular element) as long as node k does not coincide with one of the nodes attached to any of the triangular elements attached to node $\underline{\mathbf{x}}_j$. In this case the integrals appearing in Eqs. (30) and (31) are regular. Otherwise the integrals are singular and special computation is required, as discussed in Appendix B. Substituting Eqs. (24) into (23) yields

$$(\underline{\mathbf{H}} - \underline{\underline{\mathbf{G}}}\underline{\mathbf{R}})\underline{\mathscr{U}} = \underline{\mathscr{S}} - \underline{\underline{\mathbf{G}}}\underline{\mathbf{P}}. \tag{34}$$

This is a single equation to solve for all boundary nodal values of the light fluence $\underline{\mathscr{U}}$ (comprising both excitation and emission fluence).

2.2. Inhomogenous domains

2.2.1. Definition of the problem and BEM formulation

Assume that a domain volume Ω, with boundary $\partial\Omega$, comprises an inner subdomain Ω_i, with boundary $\partial\Omega_\mathrm{i}$, and outer subdomain Ω_o, with boundary $\partial\Omega_\mathrm{o} = \partial\Omega_\mathrm{i} \cup \partial\Omega$ (Fig. 1). The internal properties of the volume Ω_i are characterized by the matrices $\underline{\underline{\mathbf{D}}}_\mathrm{i}$, $\underline{\underline{\mathbf{k}}}_\mathrm{i}$ whereas the outer volume Ω_o is defined by the matrices $\underline{\underline{\mathbf{D}}}_\mathrm{o}$, $\underline{\underline{\mathbf{k}}}_\mathrm{o}$. The Robin boundary conditions (8) still apply on $\partial\Omega$. Inside each volume Ω_i (inner) and Ω_o (outer) we define $\underline{\mathbf{\Phi}}_\mathrm{i}$ and $\underline{\mathbf{\Phi}}_\mathrm{o}$ as the inner and outer light fluences defined on the boundary nodes directly touching each domain (note that nodes defining the boundary of the inner volume Ω_i are shared). Eq. (17) still holds since each volume is defined as being internally homogenous and two integral equations (inner and outer equations, respectively) can be defined as follows:

$$\underline{\mathbf{\Phi}}_\mathrm{i}(\underline{\mathbf{x}}_d) + \int_{\partial\Omega_\mathrm{i}} \left(-\underline{\underline{\mathbf{\Psi}}}_\mathrm{i}^\mathrm{T} \frac{\partial \underline{\mathbf{\Phi}}_\mathrm{i}}{\partial n_\mathrm{i}} + \frac{\partial \underline{\underline{\mathbf{\Psi}}}_\mathrm{i}^\mathrm{T}}{\partial n_\mathrm{i}} \underline{\mathbf{\Phi}}_\mathrm{i} \right) d\underline{\mathbf{x}} = \underline{\mathbf{0}} \quad \underline{\mathbf{x}}_d \in \partial\Omega_\mathrm{i}, \tag{35}$$

$$\underline{\mathbf{\Phi}}_\mathrm{o}(\underline{\mathbf{x}}_d) + \int_{\partial\Omega_\mathrm{o}} \left(-\underline{\underline{\mathbf{\Psi}}}_\mathrm{o}^\mathrm{T} \frac{\partial \underline{\mathbf{\Phi}}_\mathrm{o}}{\partial n_\mathrm{o}} + \frac{\partial \underline{\underline{\mathbf{\Psi}}}_\mathrm{o}^\mathrm{T}}{\partial n_\mathrm{o}} \underline{\mathbf{\Phi}}_\mathrm{o} \right) d\underline{\mathbf{x}} = \int_{\Omega_\mathrm{o}} \left(\underline{\underline{\mathbf{\Psi}}}_\mathrm{o}^\mathrm{T} \underline{\mathbf{S}} \right) d\underline{\mathbf{x}} \quad \underline{\mathbf{x}}_d \in \partial\Omega_\mathrm{o}. \tag{36}$$

Here, $\underline{\underline{\mathbf{\Psi}}}_\mathrm{i}$ and $\underline{\underline{\mathbf{\Psi}}}_\mathrm{o}$ are the Green matrices relative to the subdomains Ω_i and Ω_o, respectively. Note that, according to the inner normal $\vec{n}_\mathrm{i}$, the flux leaving the inner volume through the inner boundary $\partial\Omega_\mathrm{i}$ is $\underline{\underline{\mathbf{D}}}_\mathrm{i} \frac{\partial \underline{\mathbf{\Phi}}_\mathrm{i}}{\partial n_\mathrm{i}}$ whereas the flux entering the outer volume is $-\underline{\underline{\mathbf{D}}}_\mathrm{i} \frac{\partial \underline{\mathbf{\Phi}}_\mathrm{i}}{\partial n_\mathrm{o}}$. We can now define the following matching boundary conditions required at the shared nodes along the internal boundary $\partial\Omega_\mathrm{i}$

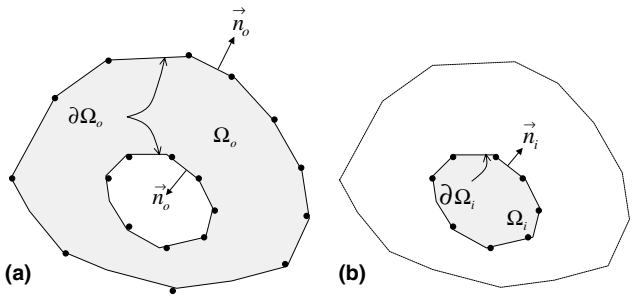

Fig. 1. Geometry and notation of inhomogeneous domain showing (a) the outer subdomain Ω_o and (b) one inner subdomain Ω_i (illustrated in 2D, for clarity).

$$\underline{\mathbf{\Phi}}_{\mathrm{i}}(\underline{\mathbf{x}}) = \underline{\mathbf{\Phi}}_{\mathrm{o}}(\underline{\mathbf{x}}), \quad \underline{\mathbf{x}} \in \partial\Omega_{\mathrm{i}}, \tag{37}$$

$$\underline{\underline{\mathbf{D}}}_{\mathrm{i}} \frac{\partial \underline{\mathbf{\Phi}}_{\mathrm{i}}(\underline{\mathbf{x}})}{\partial n_{\mathrm{i}}} = -\underline{\underline{\mathbf{D}}}_{\mathrm{o}} \frac{\partial \underline{\mathbf{\Phi}}_{\mathrm{o}}(\underline{\mathbf{x}})}{\partial n_{\mathrm{o}}}, \quad \underline{\mathbf{x}} \in \partial\Omega_{\mathrm{i}}. \tag{38}$$

These conditions impose the continuity of the light fluence (37) and the conservation of the light flux (38) at the nodes on the shared boundary $\partial\Omega_{\mathrm{i}}$. Consider a triangular mesh discretization for both the boundaries $\partial\Omega_{\mathrm{i}}$ and $\partial\Omega_{\mathrm{o}} = \partial\Omega_{\mathrm{i}} \cup \partial\Omega$. In the following, the subscript I or O indicates quantities relative to the nodes of the inner boundary $\partial\Omega_{\mathrm{i}}$ or the outer boundary $\partial\Omega_{\mathrm{o}}$, respectively, whereas the superscript (i) or (o) indicates properties relative to the inner volume Ω_{i} or outer volume Ω_{o}. We use linear elements as we did for the homogenous case (see Eq. (22)) and indicate with n_{I} and n_{O} the number of nodes of the inner and outer boundaries, respectively, and $n_{\mathrm{T}} = n_{\mathrm{I}} + n_{\mathrm{O}}$ the total number of nodes. The BEM discretization of the inner and outer equations are, respectively,

$$\underset{(2n_{\mathrm{I}}\times 2n_{\mathrm{I}})}{\underline{\underline{\mathbf{H}}}^{(\mathrm{i})}} \; \underset{(2n_{\mathrm{I}}\times 1)}{\underline{\mathscr{U}}_{\mathrm{I}}^{(\mathrm{i})}} + \underset{(2n_{\mathrm{I}}\times 2n_{\mathrm{I}})}{\underline{\underline{\mathbf{G}}}^{(\mathrm{i})}} \; \underset{(2n_{\mathrm{I}}\times 1)}{\underline{\mathscr{V}}_{\mathrm{I}}^{(\mathrm{i})}} = \underset{(2n_{\mathrm{I}}\times 1)}{\underline{\mathbf{0}}} \tag{39}$$

and

$$\underset{(2n_{\mathrm{T}}\times 2n_{\mathrm{T}})}{\underline{\underline{\mathbf{H}}}^{(\mathrm{o})}} \; \underset{(2n_{\mathrm{T}}\times 1)}{\underline{\mathscr{U}}^{(\mathrm{o})}} + \underset{(2n_{\mathrm{T}}\times 2n_{\mathrm{T}})}{\underline{\underline{\mathbf{G}}}^{(\mathrm{o})}} \; \underset{(2n_{\mathrm{T}}\times 1)}{\underline{\mathscr{V}}^{(\mathrm{o})}} = \underset{(2n_{\mathrm{T}}\times 1)}{\underline{\mathscr{S}}^{(\mathrm{o})}}, \tag{40}$$

where the sizes of matrices and vectors are shown for clarity. Here, $\underline{\mathscr{U}}^{(\mathrm{o})}$ and $\underline{\mathscr{V}}^{(\mathrm{o})}$ and $\underline{\mathscr{S}}^{(\mathrm{o})}$ are defined as follows:

$$\underset{(2n_{\mathrm{T}}\times 1)}{\underline{\mathscr{U}}^{(\mathrm{o})}} = \begin{bmatrix} \underset{(2n_{\mathrm{I}}\times 1)}{\underline{\mathscr{U}}_{\mathrm{I}}^{(\mathrm{o})}} \\ \underset{(2n_{\mathrm{O}}\times 1)}{\underline{\mathscr{U}}_{\mathrm{O}}^{(\mathrm{o})}} \end{bmatrix}, \quad \underset{(2n_{\mathrm{T}}\times 1)}{\underline{\mathscr{V}}^{(\mathrm{o})}} = \begin{bmatrix} \underset{(2n_{\mathrm{I}}\times 1)}{\underline{\mathscr{V}}_{\mathrm{I}}^{(\mathrm{o})}} \\ \underset{(2n_{\mathrm{O}}\times 1)}{\underline{\mathscr{V}}_{\mathrm{O}}^{(\mathrm{o})}} \end{bmatrix}, \quad \underset{(2n_{\mathrm{T}}\times 1)}{\underline{\mathscr{S}}^{(\mathrm{o})}} = \begin{bmatrix} \underset{(2n_{\mathrm{I}}\times 1)}{\underline{\mathbf{0}}} \\ \underset{(2n_{\mathrm{O}}\times 1)}{\underline{\mathscr{S}}_{\mathrm{O}}^{(\mathrm{o})}} \end{bmatrix}, \tag{41}$$

and $\underline{\mathscr{U}}_{\mathrm{I}}^{(\mathrm{i})}$ and $\underline{\mathscr{V}}_{\mathrm{I}}^{(\mathrm{i})}$ refer to the nodal values of the inner fluence $\underline{\mathbf{\Phi}}_{\mathrm{i}}$ and its normal derivative along the inner boundary $\partial\Omega_{\mathrm{i}}$. The vectors $\underline{\mathscr{U}}_{\mathrm{I}}^{(\mathrm{o})}$ and $\underline{\mathscr{V}}_{\mathrm{I}}^{(\mathrm{o})}$ are relative to the nodal values of the outer fluence $\underline{\mathbf{\Phi}}_{\mathrm{o}}$ and its normal derivative along the inner boundary $\partial\Omega_{\mathrm{i}}$, respectively, whereas $\underline{\mathscr{U}}_{\mathrm{O}}^{(\mathrm{o})}$ and $\underline{\mathscr{V}}_{\mathrm{O}}^{(\mathrm{o})}$ are vectors relative to the nodal values of the outer boundary $\partial\Omega_{\mathrm{o}}$. Note that both the elements of the matrices $\underline{\underline{\mathbf{H}}}^{(\mathrm{i})}$ and $\underline{\underline{\mathbf{G}}}^{(\mathrm{i})}$, as well as the matrices $\underline{\underline{\mathbf{H}}}^{(\mathrm{o})}$ and $\underline{\underline{\mathbf{G}}}^{(\mathrm{o})}$, are computed using Eqs. (30) and (31), with $\partial\Omega_{\mathrm{i}}$ and $\partial\Omega_{\mathrm{o}}$ as boundary contours for the integrations, respectively.

Because of the matching conditions (37) and (38) we need to impose the nodal conditions

$$\underline{\mathscr{U}}_{\mathrm{I}}^{(\mathrm{o})} = \underline{\mathscr{U}}_{\mathrm{I}}^{(\mathrm{i})}, \tag{42}$$

$$\underline{\underline{\mathscr{D}}}^{(\mathrm{o})} \underline{\mathscr{V}}_{\mathrm{I}}^{(\mathrm{o})} = -\underline{\underline{\mathscr{D}}}^{(\mathrm{i})} \underline{\mathscr{V}}_{\mathrm{I}}^{(\mathrm{i})}, \tag{43}$$

where $\underline{\underline{\mathscr{D}}}^{(\mathrm{o})}$ and $\underline{\underline{\mathscr{D}}}^{(\mathrm{i})}$ are block-diagonal matrices defined as follows:

$$\underset{(2n_{\mathrm{I}}\times 2n_{\mathrm{I}})}{\underline{\underline{\mathscr{D}}}^{(\mathrm{o})}} = \begin{bmatrix} \underline{\underline{\mathbf{D}}}_{\mathrm{o}} & & \\ & \cdots & \\ & & \underline{\underline{\mathbf{D}}}_{\mathrm{o}} \end{bmatrix}, \quad \underset{(2n_{\mathrm{I}}\times 2n_{\mathrm{I}})}{\underline{\underline{\mathscr{D}}}^{(\mathrm{i})}} = \begin{bmatrix} \underline{\underline{\mathbf{D}}}_{\mathrm{i}} & & \\ & \cdots & \\ & & \underline{\underline{\mathbf{D}}}_{\mathrm{i}} \end{bmatrix}. \tag{44}$$

From Eq. (39) and the matching conditions (42) and (43) we derive a relation between the vectors $\underline{\mathscr{V}^{(o)}}$ and $\underline{\mathscr{U}^{(o)}}$ that is equivalent to a discretized Robin boundary condition as in Eq. (24) for the homogenous case. Since the matrix $\underline{\underline{\mathbf{G}^{(i)}}}$ is non singular, from Eq. (39) one obtains

$$\underline{\mathscr{V}_{\mathrm{I}}^{(i)}} = -(\underline{\underline{\mathbf{G}^{(i)}}})^{-1}\underline{\underline{\mathbf{H}^{(i)}}}\,\underline{\mathscr{U}_{\mathrm{I}}^{(i)}}. \tag{45}$$

Applying the matching condition (43), Eq. (45) yields

$$\underline{\underline{\mathscr{D}^{(o)}}}\,\underline{\mathscr{V}_{\mathrm{I}}^{(o)}} = \underline{\underline{\mathscr{D}^{(i)}}}(\underline{\underline{\mathbf{G}^{(i)}}})^{-1}\underline{\underline{\mathbf{H}^{(i)}}}\,\underline{\mathscr{U}_{\mathrm{I}}^{(i)}}. \tag{46}$$

Because of the matching condition (42), the following equation holds

$$\underline{\mathscr{V}_{\mathrm{I}}^{(o)}} = (\underline{\underline{\mathscr{D}^{(o)}}})^{-1}\underline{\underline{\mathscr{D}^{(i)}}}(\underline{\underline{\mathbf{G}^{(i)}}})^{-1}\underline{\underline{\mathbf{H}^{(i)}}}\,\underline{\mathscr{U}_{\mathrm{I}}^{(o)}}. \tag{47}$$

This is a relation between the vector $\underline{\mathscr{V}_{\mathrm{I}}^{(o)}}$ of the nodal normal derivatives of the outer fluence $\underline{\mathbf{\Phi}}_{\mathrm{o}}$ and the vector $\underline{\mathscr{U}_{\mathrm{I}}^{(o)}}$ of the nodal values of the fluence $\underline{\mathbf{\Phi}}_{\mathrm{o}}$ on the inner boundary $\partial\Omega_{\mathrm{i}}$. The discretization of the Robin boundary condition on the outer boundary $\partial\Omega$ (see Eq. (8)) is defined the same as in Eq. (23) for the homogenous case, that is

$$\underline{\mathscr{V}_{\mathrm{O}}^{(o)}} = -\underline{\underline{\mathbf{R}}}\,\underline{\mathscr{U}_{\mathrm{O}}^{(o)}} + \underline{\mathbf{P}}. \tag{48}$$

Using the vector definitions (41), Eqs. (47) and (48) can be recast together in the following block form:

$$\underline{\mathscr{V}^{(o)}} = -\underline{\underline{\mathscr{R}}}\,\underline{\mathscr{U}^{(o)}} + \underline{\mathscr{P}}, \tag{49}$$

where we have defined

$$\underset{(2n_{\mathrm{T}}\times 2n_{\mathrm{T}})}{\underline{\underline{\mathscr{R}}}} = \begin{bmatrix} \left(\underline{\underline{\mathscr{D}^{(o)}}}\right)^{-1}\underline{\underline{\mathscr{D}^{(i)}}}(\underline{\underline{\mathbf{G}^{(i)}}})^{-1}\underline{\underline{\mathbf{H}^{(i)}}} & \underline{\underline{\mathbf{0}}} \\ \underline{\underline{\mathbf{0}}} & \underline{\underline{\mathbf{R}}} \end{bmatrix}, \quad \underset{(2n_{\mathrm{T}}\times 1)}{\underline{\mathscr{P}}} = \begin{bmatrix} \underline{\mathbf{0}} \\ \underline{\mathbf{P}} \end{bmatrix}. \tag{50}$$

Substituting Eq. (49) into Eq. (40) yields the following system:

$$(\underline{\underline{\mathbf{H}^{(o)}}} - \underline{\underline{\mathbf{G}^{(o)}}}\,\underline{\underline{\mathscr{R}}})\,\underline{\mathscr{U}^{(o)}} = \underline{\mathscr{S}^{(o)}} - \underline{\underline{\mathbf{G}^{(o)}}}\,\underline{\mathscr{P}}. \tag{51}$$

Eq. (51) has the same matrix structure as Eq. (34) for the homogenous case. Extension to multiple non-overlapping inner domains is straightforward.

3. Experiments

3.1. Comparison to FEM and analytical solution on a homogeneous sphere

Both the proposed BEM formulation and the FEM (see [22] for a detailed description of our vectorized finite element implementation) were implemented in Matlab Version 6.5 [39] on a 2.2 GHz Pentium IV. In order to test the proposed BEM formulation, we first consider the propagation of light through a homogenous sphere of radius Γ. Using spherical coordinates ρ, φ, and θ, for the following axisymmetric boundary conditions:

$$D_x\frac{\partial\Phi_x}{\partial n} = P_\eta(\varphi), \quad D_m\frac{\partial\Phi_m}{\partial n} = 0 \tag{52}$$

the analytical solution of the coupled equations (10) in scalar form has expression as follows (see Appendix C for derivation):

$$\Phi_x(\rho,\varphi) = \frac{P_\eta(\varphi)\mathrm{j}_\eta\left(\sqrt{\frac{-k_x}{D_x}}\rho\right)}{d_x\mathrm{j}'_\eta\left(\sqrt{\frac{-k_x}{D_x}}\Gamma\right)}, \tag{53}$$

$$\Phi_m(\rho,\varphi) = P_\eta(\varphi)\frac{\beta D_m}{\left(\frac{k_x}{D_x}-\frac{k_m}{D_m}\right)}\left[\frac{\mathrm{j}_\eta\left(\sqrt{\frac{-k_m}{D_m}}\rho\right)}{D_m\sqrt{\frac{-k_m}{D_m}}\mathrm{j}'_\eta\left(\sqrt{\frac{-k_m}{D_m}}\Gamma\right)} - \frac{\mathrm{j}_\eta\left(\sqrt{\frac{-k_x}{D_x}}\rho\right)}{D_x\sqrt{\frac{-k_x}{D_x}}\mathrm{j}'_\eta\left(\sqrt{\frac{-k_x}{D_x}}\Gamma\right)}\right]. \tag{54}$$

Here, $P_\eta(\varphi)$ are the Legendre polynomials, $\mathrm{j}_\eta(x)$ are the spherical Bessel functions of first kind of order η and $\mathrm{j}'_\eta(x)$ is the derivative of $\mathrm{j}_\eta(x)$.

The case of $\eta = 0$ corresponds to a uniform imposed flux on the surface of the sphere, and hence the analytic solution is also homogenous on the surface of the sphere, rendering this a good test case for the accuracy and stability of numerical solutions. We have solved this problem using the BEM formulation (34) on 5 cm diameter spheres with nine levels of surface mesh discretization, using triangular elements with linear basis functions. Specifications for the coarsest, medium, and finest of these nine sphere meshes are detailed in Table 1 and depicted in Fig. 2. For these experiments, we selected optical property values consistent with the background properties employed in human breast phantom studies, assuming the presence of low levels of the fluorescent contrast agent Indocyanine Green [12], as shown in Table 2, and assumed a modulation frequency of 100 MHz. The FEM discretizations used the same surface meshes as did the BEM but had additional discretization of the internal volume of the sphere into tetrahedral elements, also using linear basis functions.

Experimental measurements are referenced in order to account for instrument effects and unknown source strength [12]. For example, referencing may be accomplished by dividing all measurements by the measurement at a designated reference location, generally one with strong measured amplitude. For the homogeneous sphere problem, any variation in nodal estimates is introduced by numerical error, and hence the accuracy of referenced predictions will vary depending on the level of noise in the prediction at an arbi-

Table 1
Three of the nine mesh discretizations of the 5 cm diameter sphere

	Coarsest sphere		Medium sphere		Finest Sphere	
	FEM	BEM	FEM	BEM	FEM	BEM
Avg. node spacing (cm)	1.43	1.88	0.56	0.66	0.32	0.40
Max. node spacing (cm)	2.20	2.20	0.95	0.83	0.60	0.52
Number of nodes	53	26	873	218	4215	602

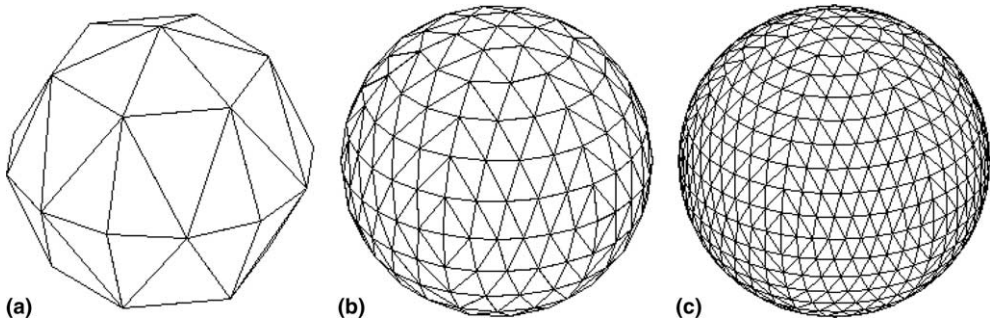

Fig. 2. The surface mesh for the (a) coarsest, (b) medium, and (c) finest discretizations of the nine sphere meshes used (see Table 1).

Table 2
Optical parameter values used in all simulations at the excitation wavelength (λ_x) and the emission wavelength (λ_m)

	μ_{af} (cm^{-1})	μ_{ai} (cm^{-1})	μ_s' (cm^{-1})	R	τ (s)	ϕ
λ_x	5.98e−3	2.48e−2	1.09e2	2.82e−2	–	–
λ_m	1.01e−3	3.22e−2	9.82e1	2.82e−2	5.6e−10	1.6e−2

trarily selected reference node. In order to minimize this sensitivity to choice of reference node for the homogeneous sphere, we instead referenced these predictions to the mean. Specifically, we divided all predicted complex fluences (Φ_x or Φ_m) for a given source by the complex mean of the nodal predictions of Φ_x or Φ_m for that source. For both the FEM and BEM, we define the prediction error as the referenced analytical solution minus the referenced numerical prediction, at all surface nodes on the sphere, for both real and imaginary components of the referenced predicted fluence (Φ_x or Φ_m). Referencing by the mean guarantees that the mean of the referenced predictions has real component equal to one and imaginary component equal to zero, so this process removes all bias from the prediction error. Consequently, the accuracy of referenced predictions on the homogeneous sphere, defined as the root mean square of the prediction error (RMSE), is equivalent to the standard deviation (σ) of the prediction error.

3.2. Comparison to FEM and experimental data from a non-homogeneous breast phantom

In order to test the BEM on a non-homogeneous domain, we compared predictions from the BEM formulation (51) to experimentally acquired measurements. In prior work [12,14–16], we experimentally collected measurements of frequency domain fluorescence emission fluence (Φ_m) from the surface of a breast shaped tissue-mimicking phantom (a 10 cm diameter hemispherical "breast" atop a 20 cm diameter cylindrical portion of the "chest wall"). Specifically, modulated excitation light at 100 MHz was used to sequentially illuminate the phantom surface (783 nm) via multimode optical fibers (1 mm diameter, model FT-1.0-EMT, Thorlabs Inc., NJ). For the data set reported here, 11 source locations were illuminated sequentially and the modulated fluorescence emission signals for each source were detected at 64 locations

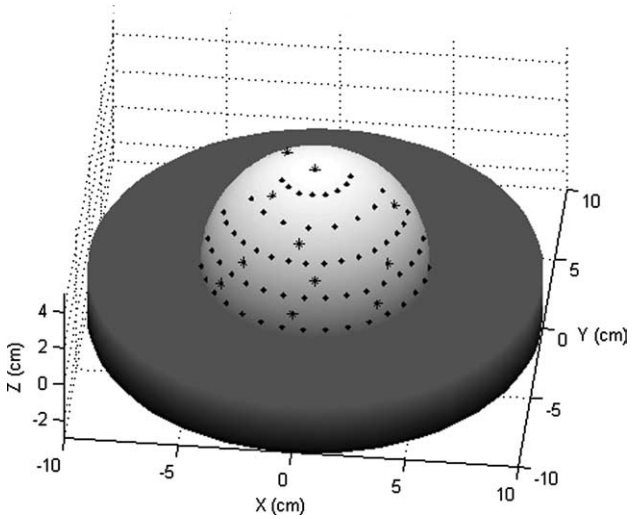

Fig. 3. Locations of the 11 sources (asterisks) and 64 detectors (black dots) on the surface of the hemispherical portion of the breast phantom, for the experimental data set presented.

on the phantom surface, as shown in Fig. 3 (detectors on the second half of the hemispherical surface were so far from the target that we did not detect any emission signal there). Thus, a total of 704 source–detector pairs (11 sources × 64 detectors) were imaged. The detected light was transmitted via multimode optical fibers to an interfacing plate that was imaged using a gain-modulated intensified charge coupled device (ICCD) camera. An optical filter assembly containing an 830-nm interference filter and a holographic notch filter was used to reject excitation light and pass fluorescent light. The transmitted fluorescent light was imaged onto the photocathode of an image intensifier (FS9910C, ITT Night Vision, VA), also modulated at 100 MHz. The resulting image on the phosphor screen of the intensifier was collected by the integrating CCD camera (CCD-512-EFT Photometric CH12, Roper Scientific, Trenton, NJ). The phosphor output was sensitive to the phase delay existing between the two phase-locked oscillators (Marconi Instruments model 2022D, UK; and Programmed Test Sources model 310M201GYX-53, Littleton, MA), modulating the incident NIR excitation light and the photocathode of the image intensifier, respectively. By varying the phase delay between the two oscillators from 0 to 2π, the steady-state intensities at each pixel of the CCD image varied sinusoidally. Fast Fourier transforms (FFT) were performed on the acquired CCD images to yield observed amplitude (I_{AC}) and phase shift (θ) of the fluorescence signal for each collection fiber, which were then converted to complex emission via $\Phi_m = I_{AC} \cdot \exp(i\theta)$. Five repetitions for each source–detector observation were collected and averaged to yield what we term the "measurements". Measurements below the noise floor of $\frac{I_{AC}}{I_{DC}} \leqslant 0.025$ were discarded. The remaining 401 measurements of complex emission fluence were referenced by dividing through by the measurement at the reference detector, specified for each source, in order to account for unknown source strength and instrument effects. A schematic of the instrumentation is shown in Fig. 4. Further details about the instrument set-up and the data acquisition procedures are provided elsewhere [12].

We have previously developed an FEM forward model for Eqs. (1) and (2) [22]. By incorporating this FEM model, using the 6956 node mesh shown in Fig. 5(a), into the Bayesian approximate extended Kalman filter image reconstruction algorithm [11,12,28,29], we have previously performed 3D tomographic reconstructions of both fluorescence absorption (μ_{axf}) [12,14,15] and fluorescence lifetime (τ) [16] using experimentally collected data from the breast phantom. These previous results indicate that the FEM

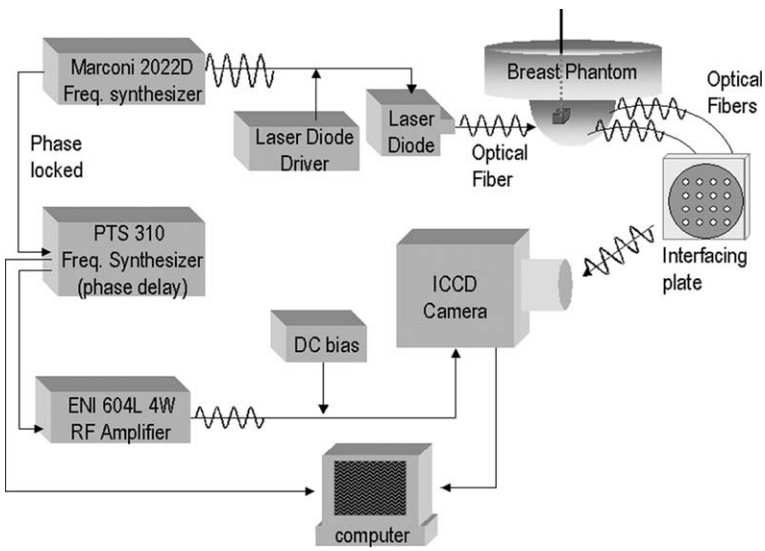

Fig. 4. Schematic of the instrumentation used for data collection. See text for details.

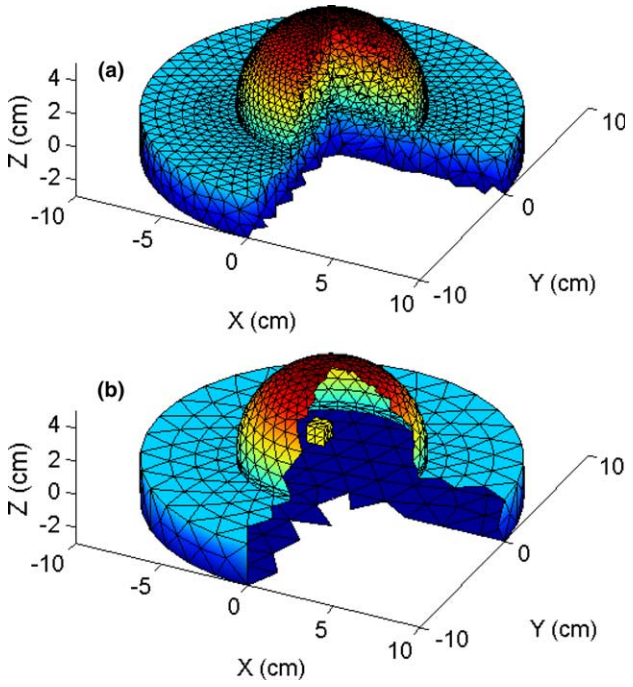

Fig. 5. Cut-away views of the discretizations used for the breast phantom simulations: (a) 6956 node finite element mesh, and (b) 708 node boundary element mesh showing internal target. See Table 4 for additional specifications.

forward model mismatch (which lumps measurement error and model error) is sufficiently low to permit identification and localization of 1 cc embedded fluorescent targets, although our FEM reconstructions are not quantitatively accurate. In lieu of an analytic solution for these heterogeneous domains, we herein compare the forward model mismatch of the BEM to that of the FEM on an experimentally acquired data set [12], with background optical properties as shown in Table 2, and a 1 cc fluorescent target with 100:1 target:background contrast in μ_{axf}, with centroid located 1.4 cm from the surface of the phantom breast. Since the BEM is more memory demanding than the FEM, using the boundary nodes of the mesh shown in Fig. 5(a) for the BEM is not computationally practical with our current computational resources. Consequently, we implemented a much coarser 708 boundary node BEM mesh to model the breast phantom (26 of these nodes were used to model the boundary of the embedded target), as shown in Fig. 5(b). The internode spacing of the 682 BEM nodes on the domain surface is approximately double that of the 2339 boundary nodes in the FEM. Note that the geometry and location of the cubic target can be very accurately represented in even when a course BEM external surface mesh is imposed, because (a) the surface mesh of the internal target is independent of the coarseness of the mesh on the outer domain surface, and (b) the shape of the internal surface is not constrained by the locations of nodes in an internal volume discretization, as in the FEM. We remind the reader that in this manuscript we are only addressing the forward problem, where the target location, size, and shape are known. In the inverse problem, the locations of internal target surface nodes could be iteratively estimated, as discussed in Section 1 (e.g., as in [36]).

FEM and BEM predictions were referenced in the same manner as the experimental measurements. Model mismatch is defined as the real and imaginary components of the referenced measured Φ_m minus the referenced predicted Φ_m. The mean of the model mismatch is an indication of bias in the combined model and measurement error. The variance of the model mismatch is a measure of the noise level in the combined model and measurement error.

4. Results

4.1. Comparison to analytical sphere solutions

In comparison to the analytical solution on the homogeneous sphere using biologically realistic optical properties, the BEM was over an order of magnitude more accurate than the FEM, due to the additional discretization error incurred by the FEM caused by the internal volume mesh required for this method. For example, in Fig. 6 we show the referenced predictions of emission fluence on the finest sphere mesh used, where it is apparent that the BEM solution is much smoother than the FEM. Consequently, bias in FEM predictions is much more sensitive to choice of a specific node for referencing; by referencing by the mean, as described in Section 3.1, we avoid this problem by explicitly eliminating all bias. Convergence of the referenced predictions of both Φ_x and Φ_m improves more rapidly with the BEM than with the FEM as the meshes become more refined. This is evidenced by the steeper slopes of the BEM convergence curves shown in Fig. 7. Note that BEM predictions of emission fluence, using all but the coarsest mesh, outperform FEM predictions with even the finest mesh.

4.2. Comparison to experimental data from breast phantom

Referenced predictions of emission fluence from the FEM with the fine mesh (Fig. 5(a)) and the BEM with the coarser mesh (Fig. 5(b)), exhibited similar model mismatch when compared to experimental results on the non-homogeneous breast phantom. In Fig. 8, we illustrate FEM and BEM predictions, relative to emission measurements, for one of the 11 source illuminations. Here it can be seen that, for some measurements, the FEM matches the data more closely than the BEM, and for other measurements the BEM matches the data more closely. Some measurements are clearly outliers with large measurement error that add to the model mismatch, but without a priori knowledge of the true domain one would not know this, so we have left them in. On average, over all 11 sources (401 source–detector pairs), the distribution of the observed model mismatch was very similar for both FEM and BEM predictions of real and imaginary components of emission fluence, as shown in Fig. 9, and quantified in Table 3. Although the inter-node spacing

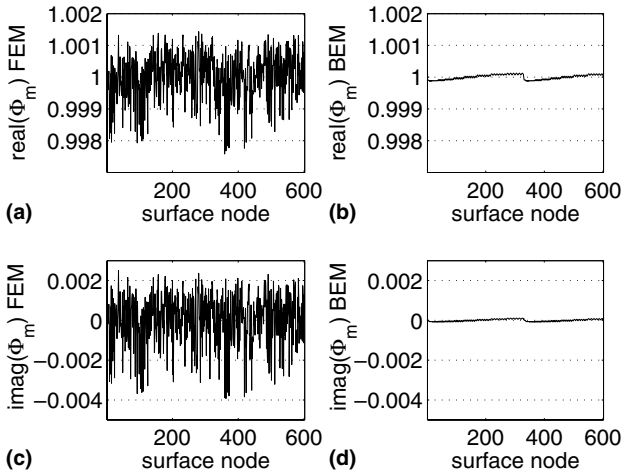

Fig. 6. FEM (a,c) and BEM (b,d) referenced predictions for the real (a,b) and imaginary (c,d) components of emission fluence, at all surface nodes on the finest sphere (Fig. 2(c), Table 1). Perfect referenced predictions would be a horizontal line at 1.0 for the real components (a,b) and a horizontal line at 0.0 for the imaginary components (c,d).

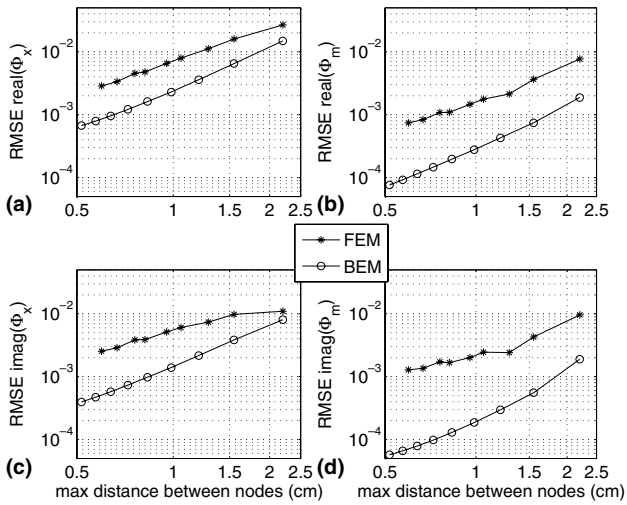

Fig. 7. Accuracy of FEM and BEM referenced predictions of real (a,b) and imaginary (c,d) components of excitation (a,c) and emission (b,d) fluence on the homogeneous sphere, as a function of sphere discretization. Here, RMSE is the root mean square of the referenced analytical solutions minus referenced predictions.

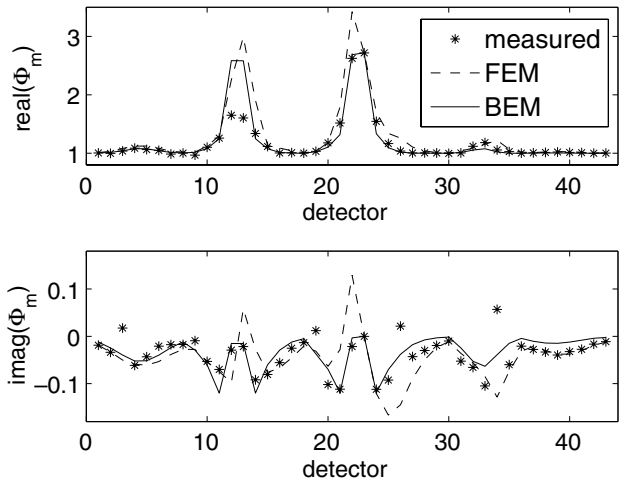

Fig. 8. (a) Real and (b) imaginary components of predicted and observed emission fluence at all detector locations for one source illumination. See Fig. 9 and Table 3 for summary statistics on all 11 sources.

on the domain surface in the BEM mesh was approximately double that of the FEM mesh (Fig. 5), the bias and variance of the BEM predictions were actually lower than those from FEM predictions (Table 3).

The FEM system matrices are large and sparse, while the BEM system matrix is relatively small but $\frac{3}{4}$ dense (see Eq. (33)). In fact, although the BEM breast mesh had an order of magnitude fewer nodes than the FEM mesh, it had an order of magnitude more non-zero elements in its system matrix (Table 4), thus requiring more memory. Despite this, total prediction time for all 11 source illuminations on the breast model took about half the time with the BEM than with the FEM. If the portions of the system matrix associated with the outer surface mesh ($\underline{\underline{\mathbf{H}}}^{(o)}$ and $\underline{\underline{\mathbf{G}}}^{(o)}$) were pre-computed, the BEM only took one eighth

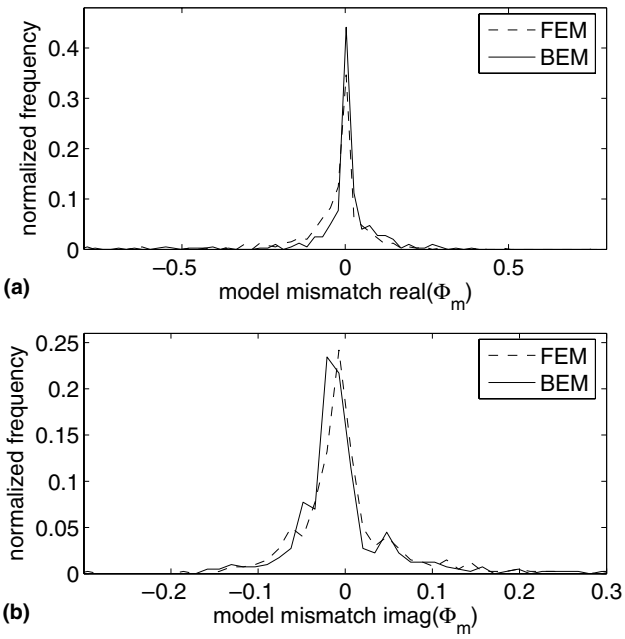

Fig. 9. Observed frequency distribution of (a) real and (b) imaginary components of model mismatch of (measured–predicted) Φ_m, for all 401 source–detector pairs on the non-homogeneous breast phantom, using the meshes shown in Fig. 5. If there were no measurement or model error the distributions would be a vertical spike at 0 of height 1.0.

Table 3
Error metrics for FEM and BEM predictions of real and imaginary components emission fluence, as compared to measured data on the breast phantom; mean (a.k.a., bias) and variance are reported for referenced (measured–predicted) Φ_m from 401 source–detector pairs (all 11 sources) (see Fig. 7)

	Bias real (Φ_m)	Variance real (Φ_m)	Bias imag (Φ_m)	Variance imag (Φ_m)
FEM	−0.0313[a]	0.0226	−0.0048	0.0072
BEM	−0.0040[a]	0.0153	−0.0044	0.0033

[a] $p < 0.001$, paired t-test.

Table 4
Computational requirements of two breast meshes used (Fig. 3)

Breast mesh	Nodes	Elements	Non-zeros	Runtime (s)
FEM	6956	34,413	188,732	139
BEM	708	1408	1,503,792	67 (17[a])

[a] With pre-computation of outer mesh.

the time of the FEM (Table 4). Pre-computing the outer surface mesh may be a practical approach in a BEM tomography application where the background properties and geometry of outer domain are held constant, and only the locations, sizes, shapes, and values of internal targets are estimated. Since this was a prototype implementation of the BEM and used a direct solver, we anticipate that further implementation improvements will yield additional speedups for the BEM.

5. Summary and conclusions

Finite element method (FEM) approaches to fluorescence tomography in clinically relevant volumes have proven feasible [12,14–16], but are highly underdetermined. Consequently, FEM-based tomographic reconstructions are dependent on, and sensitive to, regularization schemes. In contrast, boundary element method (BEM) based tomography may afford high resolution imaging of internal targets, in the context of an overdetermined problem. While FEM models may be necessary for modeling domains with a large degree of continuously varying heterogeneity, the BEM method is appropriate for applications in which the domain can be modeled with a small number of homogeneous subdomains. One such potential application is when modeling fluorescence from molecularly targeting dyes that exhibit highly localized spatial accumulation (e.g., on discrete tumors). Using the BEM, only the external boundary and the internal target boundaries require discretization, and regional solutions are solved analytically. The BEM can accurately model the geometries of internal subdomains, independent of the degree of surface discretization. Unfortunately, the application of a BEM forward model to the fluorescence diffusion equations is not straightforward, because of the internally distributed fluorescent emission source caused by embedded fluorophore.

In this contribution, we have developed a 3D BEM formulation that allows the simultaneous solution of the excitation and emission equations that describe the generation and propagation of fluorescent light through turbid media, without the need for an internal volume mesh. This formulation is based on a derivation of the fundamental solution to the coupled system of excitation and emission equations. The BEM is shown to be more accurate and more stable than the FEM, when compared to an analytic solution on a spherical homogeneous domain using optical properties consistent with those of biological tissues, owing to the lower internal discretization error inherent in the BEM. For a given inter-node spacing in the mesh, the BEM requires more memory and runtime than the FEM. However, the BEM with a coarser mesh gives more accurate and stable results, and takes less computer time, than the FEM with a fine mesh. Emission fluence predictions made with the BEM using a 708-node boundary mesh, with roughly double the inter-node spacing of boundary nodes as in a 6956-node FEM volume mesh, match experimental frequency-domain fluorescence emission measurements acquired on a non-homogeneous 1087 cm^3 breast-mimicking phantom at least as well as those of the FEM, but required only 1/8 to 1/2 the computation time. These encouraging results on the BEM forward model of fluorescence photon migration motivate us to pursue BEM-based fluorescence tomography in future work.

Acknowledgments

This work was supported in part by NIH R01 EB 002763 and the Vermont Genetics Network through NIH 1 P20 RR16462 from the BRIN program of the NCRR.

Appendix A. Analytical derivation of the Green matrix $\underline{\underline{\Psi}}$

A modal decomposition procedure is applied to solve for the fundamental solution ($\underline{\underline{\Psi}}$) of the coupled adjoint system (15), as follows. Set $\underline{\underline{\tilde{\mathbf{K}}}} = \underline{\underline{\mathbf{K}^{\mathrm{T}}}}$ in Eq. (15) as

$$\underline{\underline{\tilde{\mathbf{K}}}} = \begin{bmatrix} \tilde{K}_x & \tilde{K}_{xm} \\ 0 & \tilde{K}_m \end{bmatrix},$$

where

$$\tilde{K}_x = \frac{k_x}{D_x}, \quad \tilde{K}_{xm} = -\frac{\beta}{D_m}, \quad \tilde{K}_m = \frac{k_m}{D_m}.$$

In order to solve the adjoint system (15), define a generic non-singular matrix $\underline{\underline{\mathbf{V}}}$ and the variable transformation

$$\underline{\underline{\mathbf{\Psi}}} = \underline{\underline{\mathbf{V}}}\,\underline{\underline{\mathbf{U}}}. \tag{A.1}$$

The new differential equation satisfied by the transformed variable $\underline{\underline{\mathbf{U}}}$ is readily derived from Eq. (10) as follows:

$$\nabla^2\underline{\underline{\mathbf{U}}} - (\underline{\underline{\mathbf{V}}}^{-1}\underline{\underline{\tilde{\mathbf{K}}}}\,\underline{\underline{\mathbf{V}}})\underline{\underline{\mathbf{U}}} + \underline{\underline{\mathbf{V}}}^{-1}\underline{\underline{\Delta_j}} = \underline{\underline{\mathbf{0}}}. \tag{A.2}$$

We now choose $\underline{\underline{\mathbf{V}}}$ to be the matrix having as column entries the eigenvectors of the matrix $\underline{\underline{\tilde{\mathbf{K}}}}$. It follows that $\underline{\underline{\mathbf{V}}}^{-1}\underline{\underline{\tilde{\mathbf{K}}}}\,\underline{\underline{\mathbf{V}}} = \underline{\underline{\mathbf{\Lambda}}}$ with $\underline{\underline{\mathbf{\Lambda}}}$ the diagonal matrix of the eigenvalues and Eq. (A.2) simplifies

$$\nabla^2\underline{\underline{\mathbf{U}}} - \underline{\underline{\mathbf{\Lambda}}}\,\underline{\underline{\mathbf{U}}} + \underline{\underline{\mathbf{V}}}^{-1}\underline{\underline{\Delta_j}} = \underline{\underline{\mathbf{0}}}. \tag{A.3}$$

Here,

$$\underline{\underline{\mathbf{\Lambda}}} = \begin{bmatrix} \tilde{K}_x & 0 \\ 0 & \tilde{K}_m \end{bmatrix}, \quad \underline{\underline{\mathbf{V}}} = \begin{bmatrix} 1 & \alpha \\ 0 & 1 \end{bmatrix}, \quad \underline{\underline{\mathbf{V}}}^{-1} = \begin{bmatrix} 1 & -\alpha \\ 0 & 1 \end{bmatrix}, \tag{A.4}$$

where

$$\alpha = \frac{\tilde{K}_{xm}}{\tilde{K}_m - \tilde{K}_x} = \frac{\frac{\beta}{D_m}}{\frac{k_x}{D_x} - \frac{k_m}{D_m}}. \tag{A.5}$$

From the matrix equation (A.3) the following scalar equations for the entries U_{ij} of the matrix $\underline{\underline{\mathbf{U}}}$ can be derived

$$\begin{aligned} &\nabla^2 U_{11} - \tilde{K}_x U_{11} + \delta(\rho) = 0, \\ &\nabla^2 U_{12} - \tilde{K}_x U_{12} - \alpha\delta(\rho) = 0, \\ &\nabla^2 U_{21} + \tilde{K}_m U_{21} = 0, \\ &\nabla^2 U_{22} - \tilde{K}_m U_{22} + \delta(\rho) = 0. \end{aligned} \tag{A.6}$$

Note that the component U_{21} is zero and the analytical expression of the matrix $\underline{\underline{\mathbf{U}}}$ is readily obtained as

$$\underline{\underline{\mathbf{U}}} = \begin{bmatrix} G\left(\sqrt{-\tilde{K}_x}\rho\right) & -\alpha G\left(\sqrt{-\tilde{K}_x}\rho\right) \\ 0 & G\left(\sqrt{-\tilde{K}_m}\rho\right) \end{bmatrix}, \tag{A.7}$$

where $G(\sqrt{-\lambda}r)$ satisfies the Helmholtz-type equation

$$\nabla^2 G - \lambda G + \delta(\rho) = 0, \quad \lambda = \tilde{K}_x, \tilde{K}_m. \tag{A.8}$$

The following radiation boundary condition at infinity needs to be satisfied in order to guarantee decay-outgoing solutions from the location $\underline{\mathbf{x}} = \underline{\mathbf{x}}_j$, i.e.,

$$\lim_{\rho\to\infty}\left(\frac{\partial G}{\partial \rho} - \mathrm{i}\sqrt{-\lambda}G\right) = 0. \tag{A.9}$$

In two dimensions

$$G(\sqrt{-\lambda}\rho) = \frac{\mathrm{i}}{4} H_0^1\left(\sqrt{-\lambda}\rho\right), \tag{A.10}$$

where $H_0^1(x)$ is the Hankel function of first kind and order 0, whereas in three dimensions

$$G(\sqrt{-\lambda}\rho) = \frac{1}{4\pi\rho} \exp\left(\mathrm{i}\sqrt{-\lambda}\rho\right). \tag{A.11}$$

Using the transformation (A.1) the Green matrix $\underline{\underline{\boldsymbol{\Psi}}}$ has the general expression as follows:

$$\underline{\underline{\boldsymbol{\Psi}}} = \begin{bmatrix} G\left(\sqrt{-\tilde{K}_x}\rho\right) & -\alpha G\left(\sqrt{-\tilde{K}_x}\rho\right) + \alpha G\left(\sqrt{-\tilde{K}_m}\rho\right) \\ 0 & G\left(\sqrt{-\tilde{K}_m}\rho\right) \end{bmatrix}. \tag{A.12}$$

Appendix B. Computation of the matrices $\underline{\underline{\mathbf{H}}}$ and $\underline{\underline{\mathbf{G}}}$

Eqs. (30) and (31) are required to compute the element entries of the matrices $\underline{\underline{\mathbf{H}}}$ and $\underline{\underline{\mathbf{G}}}$ (Eqs. (29)), and are repeated below:

$$\underset{(2\times 2)}{\underline{\underline{\mathbf{h}}}_{jk}} = \delta_{jk} \underset{(2\times 2)}{\underline{\underline{\mathbf{I}}}} + \int_{\partial\Omega} \frac{\partial \underline{\underline{\boldsymbol{\Psi}}}^{\mathrm{T}}}{\partial n} N_k(\underline{\mathbf{x}})\, \mathrm{d}\underline{\mathbf{x}}, \tag{B.1}$$

$$\underset{(2\times 2)}{\underline{\underline{\mathbf{g}}}_{jk}} = -\int_{\partial\Omega} \underline{\underline{\boldsymbol{\Psi}}}^{\mathrm{T}} N_k(\underline{\mathbf{x}})\, \mathrm{d}\underline{\mathbf{x}}. \tag{B.2}$$

Special computation is required if the node k coincides with one of the nodes attached to any of the triangular elements attached to node $\underline{\mathbf{x}}_j$. In this case, Gauss quadrature gives poor approximations. In order to compute these integrals, we set a polar coordinate system (ρ, θ) at $\underline{\mathbf{x}}_j$. Since $\rho = |\underline{\mathbf{x}} - \underline{\mathbf{x}}_j|$, Eqs. (B.1) and (B.2), in the polar system, transform to

$$\underset{(2\times 2)}{\underline{\underline{\mathbf{h}}}_{jk}} = \delta_{jk} \underset{(2\times 2)}{\underline{\underline{\mathbf{I}}}} + \int_{\partial\Omega} \frac{\partial \underline{\underline{\boldsymbol{\Psi}}}^{\mathrm{T}}}{\partial \rho} \frac{\partial \rho}{\partial n} N_k(\rho, \theta) \rho\, \mathrm{d}\rho\, \mathrm{d}\theta, \tag{B.3}$$

$$\underset{(2\times 2)}{\underline{\underline{\mathbf{g}}}_{jk}} = -\int_{\partial\Omega} \underline{\underline{\boldsymbol{\Psi}}}^{\mathrm{T}} N_k(\rho, \theta) \rho\, \mathrm{d}\rho\, \mathrm{d}\theta. \tag{B.4}$$

Here, the integral in (B.4) is regular, since $\underline{\underline{\boldsymbol{\Psi}}} \sim \frac{1}{\rho}$ and can be easily computed by numerical quadrature in the domain (ρ, θ). The integral in (B.3) is weakly singular, since $\frac{\partial \underline{\underline{\boldsymbol{\Psi}}}}{\partial \rho} \sim \frac{1}{\rho^2}$. In order to compute it, we consider an external small spherical surface $\partial\Omega_\epsilon$ of radius ϵ centered at node $\underline{\mathbf{x}}_j$ (Fig. 10). The integral splits into two components, as follows:

$$\underset{(2\times 2)}{\underline{\underline{\mathbf{h}}}_{jk}} = \delta_{jk} \underset{(2\times 2)}{\underline{\underline{\mathbf{I}}}} + \int_{\partial\Omega_\epsilon} \frac{\partial \underline{\underline{\boldsymbol{\Psi}}}^{\mathrm{T}}}{\partial \rho} \frac{\partial \rho}{\partial n} N_k(\rho, \theta) \rho\, \mathrm{d}\rho\, \mathrm{d}\theta + \int_{\partial\Omega \setminus \partial\Omega_\epsilon} \frac{\partial \underline{\underline{\boldsymbol{\Psi}}}^{\mathrm{T}}}{\partial \rho} \frac{\partial \rho}{\partial n} N_k(\rho, \theta) \rho\, \mathrm{d}\rho\, \mathrm{d}\theta. \tag{B.5}$$

Note that the second component of (B.5) vanishes, since $\frac{\partial \rho}{\partial n} = 0$ in $\partial\Omega \setminus \partial\Omega_\epsilon$. Consequently, the integral simplifies as follows:

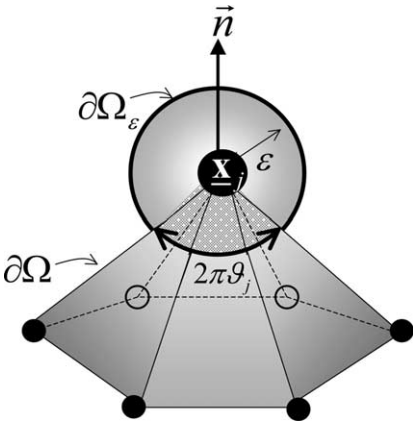

Fig. 10. Local geometry of a node, showing the spherical surface $\partial\Omega_\epsilon$ centered at node $\underline{\mathbf{x}}_j$, and the internal solid angle ϑ_j, described in Appendix B.

$$\underset{(2\times2)}{\underline{\underline{\mathbf{h}}}}_{jk} = \delta_{jk}\underset{(2\times2)}{\underline{\underline{\mathbf{I}}}} + \int_{\partial\Omega_\epsilon} \frac{\partial \underline{\underline{\boldsymbol{\Psi}}}^{\mathrm{T}}}{\partial\rho} N_k(\rho,\theta)\rho \,\mathrm{d}\rho \,\mathrm{d}\theta. \tag{B.6}$$

In the limit as $\epsilon \to 0$, it holds that $N_k(\rho,\theta) \to \delta_{jk} + \mathrm{o}(\epsilon)$, and (B.6) simplifies to:

$$\underset{(2\times2)}{\underline{\underline{\mathbf{h}}}}_{jk} = \delta_{jk}\underset{(2\times2)}{\underline{\underline{\mathbf{I}}}}(1-\vartheta_j) + \mathrm{o}(\epsilon). \tag{B.7}$$

Here, $4\pi\vartheta_j$ is the internal solid angle in steradians, with respect to the normal direction facing the outside of the boundary $\partial\Omega$ at the node $\underline{\mathbf{x}}_j$ (Fig. 10). If the surface is flat then $\vartheta_j = \frac{1}{2}$.

Appendix C. Analytic solution to homogeneous domain

We derived the analytic solution of the coupled system (10) as follows. Using a similar procedure as applied to derive the Green matrix as described in Appendix A, one can obtain the following eigenfunction expansion for the equations in system (10). Using spherical coordinates ρ, φ, and θ,

$$\Phi_x(\rho,\varphi,\theta) = \sum A_{\eta\zeta} \exp(\mathrm{i}\zeta\theta) P_\eta^\zeta(\varphi) \mathrm{j}_\eta\left(\sqrt{-\frac{k_x}{D_x}}\rho\right), \tag{C.1}$$

$$\Phi_m(\rho,\varphi,\theta) = \sum \exp(\mathrm{i}\zeta\theta) P_\eta^\zeta(\varphi)\left[B_{\eta\zeta}\mathrm{j}_\eta\left(\sqrt{-\frac{k_m}{D_m}}\rho\right) - \chi A_{\eta\zeta}\mathrm{j}_\eta\left(\sqrt{-\frac{k_x}{D_x}}\rho\right)\right]. \tag{C.2}$$

Here, $A_{\eta\zeta}$ and $B_{\eta\zeta}$ depend upon the boundary conditions, $P_\eta^\zeta(\varphi)$ are the Legendre functions (for $\zeta = 0$ they become the Legendre polynomials $P_\eta(\varphi)$), $\mathrm{j}_\eta(x)$ is the spherical Bessel function of first kind of order η

$$\mathrm{j}_\eta(x) = \frac{J_{(\eta+\frac{1}{2})}(x)}{\sqrt{x}}, \tag{C.3}$$

where $J_\eta(x)$ is the Bessel function of first kind of order η. The parameter χ is defined as follows:

$$\chi = \frac{\beta D_m}{\left(\frac{k_x}{D_x} - \frac{k_m}{D_m}\right)}.$$

The boundary conditions (52) impose axisymmetry, i.e., $\zeta = 0$, and from Eqs. (C.1) and (C.2) the two following equations are obtained:

$$A_\eta D_x \sqrt{-\frac{k_x}{D_x}}\mathrm{j}'_\eta\left(\sqrt{-\frac{k_x}{D_x}}\rho\right) = 1, \tag{C.4}$$

$$B_\eta \sqrt{-\frac{k_m}{D_m}}\mathrm{j}'_\eta\left(\sqrt{-\frac{k_m}{D_m}}\rho\right) - \chi A_\eta \sqrt{-\frac{k_x}{D_x}}\mathrm{j}'_\eta\left(\sqrt{-\frac{k_x}{D_x}}\rho\right) = 0, \tag{C.5}$$

where $\mathrm{j}'_\eta(x)$ is the derivative of $\mathrm{j}_\eta(x)$. Then one can solve for the coefficients A_η and B_η and the solutions for the homogeneous sphere (53) and (54) are readily derived.

References

[1] S. Folli, P. Westerman, D. Braichotte, A. Pelegrin, G. Wagnieres, H. Van den Berg, J.P. Mach, Antibody-indocyanin conjugates for immunophotodetection of human squamous cell carcinoma in nude mice, Cancer Res. 54 (1994) 2643–2649.

[2] B. Neri, B. Carnemolla, A. Nissim, A. Leprini, G. Querze, E. Balza, A. Pini, L. Tarli, C. Halin, P. Neri, L. Zardi, G. Winter, Targeting by affinity-matured recombinant antibody fragments of an angiogenesis associated fibronectin isoform, Nat. Biotechnol. 15 (1997) 1271–1275.

[3] E. Schellenberger, A. Bogdanov, A. Petrovsky, V. Ntziachristos, R. Weissleder, L. Josephson, Optical imaging of apoptosis as a biomarker of tumor response to chemotherapy, Neoplasia 5 (2003) 187–192.

[4] S. Achilefu, R.B. Dorshow, J.E. Bugah, R. Rajagopalan, Novel receptor-targeted fluorescent contrast agents for in vivo tumor imaging, Invest. Radiol. 35 (2000) 479–485.

[5] A. Becker, C. Hessenius, K. Licha, B. Ebert, U. Sukowski, W. Semmler, B. Wiedenmann, C. Grotzinger, Receptor-targeted optical imaging of tumors with near-infrared fluorescent ligands, Nat. Biotechnol. 19 (2001) 327–331.

[6] R. Weissleder, C.H. Tung, U. Mahmood, A. Bogdanov, In vivo imaging of tumors with protease-activated near-infrared fluroescent probes, Nat. Biotechnol. 17 (1999) 375–378.

[7] S. Tyagi, F.R. Kramer, Molecular beacons: probes that fluorescence upon hybridization, Nat. Biotechnol. 14 (1996) 303–308.

[8] V. Ntziachristos, R. Weissleder, Experimental three-dimensional fluorescence reconstruction of diffuse media using normalized Born approximation, Opt. Lett. 26 (2001) 893–895.

[9] V. Ntziachristos, C. Tung, C. Bremer, R. Weissleder, Fluorescence-mediated tomography resolves portease activity in vivo, Nat. Med. 8 (2002) 757–760.

[10] V. Chenomordik, D. Hattery, I. Gannot, A.H. Gandjbakhche, Inverse method 3-D reconstruction of localized in vivo fluorescence – application to Sjogren syndrome, IEEE J. Sel. Top. Quantum Electron. 54 (1999) 930–935.

[11] M.J. Eppstein, D.J. Hawrysz, A. Godavarty, E.M. Sevick-Muraca, Three-dimensional, Bayesian image reconstruction from sparse and noisy data sets: near-infrared fluorescence tomography, Proc. Natl. Acad. Sci. USA 99 (15) (2002) 9619–9624.

[12] A. Godavarty, M.J. Eppstein, C. Zhang, A.B. Thompson, M. Gurfinkel, S. Theru, E.M. Sevick-Muraca, Fluorescence-enhanced optical imaging in large tissue volumes using a gain modulated ICCD camera, Phys. Med. Biol. 48 (2003) 1701–1720.

[13] R. Roy, A. Godavarty, E.M. Sevick-Muraca, Fluorescence-enhanced optical tomography using referenced measurements of heterogeneous media, IEEE Trans. Med. Imaging 22 (7) (2003) 824–836.

[14] A. Godavarty, C. Zhang, M.J. Eppstein, E.M. Sevick-Muraca, Fluorescence-enhanced optical imaging of large phantoms using single and dual source systems, Med. Phys. 31 (2) (2004) 183–190.

[15] A. Godavarty, M.J. Eppstein, C. Zhang, E.M. Sevick-Muraca, Detection of multiple targets in breast phantoms using fluorescence-enhanced optical imaging, Radiology 235 (2005) 148–154.

[16] A. Godavarty, E.M. Sevick-Muraca, M.J. Eppstein, Three-dimensional fluorescence lifetime tomography, Med. Phys. 32 (4) (2005) 992–1000.

[17] E.M. Sevick-Muraca, A. Godavarty, J.P. Houston, A.B. Thompson, R. Roy, Near-infrared imaging with fluorescent contrast agents, in: B. Pogue, M.A. Mycek (Eds.), Fluorescence in Biomedicine, Marcel-Dekker, New York, 2003.

[18] M.S. Patterson, B.W. Pogue, Mathematical model for time-resolved and frequency-domain fluorescence spectroscopy in biological tissues, Appl. Opt. 33 (1994) 1963.

[19] E.M. Sevick-Muraca, C.L. Burch, Origin of phosphorescence signals re-emitted from tissues, Opt. Lett. 19 (1994) 1928.
[20] C.L. Hutchinson, T.L. Troy, E.M. Sevick-Muraca, Fluorescence-lifetime determination in tissues or other scattering media from measurement of excitation and emission kinetics, Appl. Opt. 35 (1996) 2325.
[21] H. Jiang, Frequency-domain fluorescent diffusion tomography: a finite-element-based algorithm and simulations, Appl. Opt. 37 (22) (1998) 5337–5343.
[22] F. Fedele, J.P. Laible, M.J. Eppstein, Coupled complex adjoint sensitivities for frequency-domain fluorescence tomography: theory and vectorized implementation, J. Comput. Phys. 187 (2003) 597–619.
[23] S.R. Arridge, Optical tomography in medical imaging, Inv. Prob. 15 (1999) R41–R93.
[24] B.W. Pogue, T.O. McBride, J. Prewitt, U.L. Osterberg, K.D. Paulsen, Spatially variant regularization improves diffuse optical tomography, Appl. Opt. 38 (1999) 2950–2961.
[25] J.C. Ye, K.J. Webb, C.A. Bouman, R.P. Millane, Optical diffusion tomography by iterative-coordinate-descent optimization in a Bayesian framework, J. Opt. Soc. Am. A 16 (1999) 2400–2412.
[26] A.H. Hielscher, S. Bartel, Use of penalty terms in gradient-based iterative reconstruction schemes for optical tomography, J. Biomed. Opt. 6 (2) (2001) 183–192.
[27] B.W. Pogue, K.D. Paulsen, High-resolution near-infrared tomgraphic imaging simulations of the rat cranium by use of a priori magnetic resonance imaging structural information, Opt. Lett. 23 (21) (1998) 1716.
[28] M.J. Eppstein, D.E. Dougherty, T.L. Troy, E.M. Sevick-Muraca, Biomedical optical tomography using dynamic parameterization and Bayesian conditioning on photon migration measurements, Appl. Opt. 38 (1999) 2138–2150.
[29] M.J. Eppstein, D.E. Dougherty, D.J. Hawrysz, E.M. Sevick-Muraca, 3-D Bayesian optical image reconstruction with domain decomposition, IEEE Trans. Med. Imaging 20 (3) (2001) 147–163.
[30] A. Joshi, A.B. Thompson, E.M. Sevick-Muraca, W. Bangerth, Adaptive finite element methods for forward modeling in fluorescence enhanced frequency domain optical tomography, OSA Biomedical Topical Meetings, OSA Technical Digest, Optical Society of America, Washington, DC, paper WB7, April, 2004.
[31] C. Brebbia, The Boundary Element Method for Engineers, Penntech Press, 1978.
[32] E.E. Graves, J. Ripoll, R. Weissleder, V. Ntziachristos, A submillimeter resolution fluorescence molecular imaging system for small animal imaging, Med. Phys. 30 (5) (2003) 901–911.
[33] M. Moseley, G. Donnan, Multimodality imaging: introduction, Stroke 35 (2004) 2632–2634.
[34] S. Kim, Y.T. Lim, E.G. Soltesz, A.M. De Grand, J. Lee, A. Nakayama, J.A. Parker, T. Mihaljevic, R.G. Laurence, D.M. Dor, L.H. Cohn, M.G. Bawendi, J.V. Frangioni, Near-infrared fluorescent type II quantum dots for sentinel lymph node mapping, Nat. Biotechnol. 22 (2003) 93–97.
[35] J.C. De Munck, T.J.C. Faes, R.M. Heethaar, The boundary element method in the forward and inverse problem of electrical impedance tomography, IEEE Trans. Biomed. Eng. 47 (2000) 792–800.
[36] C.-T. Hsiao, G. Chahine, N. Gumerov, Application of a hybrid genetic/Powell algorithm and a boundary element method to electrical impedance tomography, J. Comput. Phys. 173 (2001) 433–454.
[37] D.S. Broomhead, D. Lowe, Multivariate functional interpolation and adaptive networks, Complex Syst. 2 (1988) 321–355.
[38] J. Heino, S. Arridge, J. Sikora, E. Somersalo, Anisotropic effects in highly scattering media, Phys. Rev. E 68 (2003) 031908 (8pp).
[39] The Mathworks, 24 Prime Park Way, Natick, MA 01760-1500.